Realia et naturalia

DISSERTATIONES
PHYSICAE
UNIVERSITATIS
TARTUENSIS
92

DEIVID PUGAL

hp-FEM model of IPMC deformation

DISSERTATIONES PHYSICAE UNIVERSITATIS TARTUENSIS
92

DISSERTATIONES PHYSICAE UNIVERSITATIS TARTUENSIS
92

DEIVID PUGAL

hp-FEM model of IPMC deformation

UNIVERSITY OF TARTU
PRESS
1632

Institute of Physics, University of Tartu, Estonia

The Dissertation was admitted on February 2nd, 2014 in partial fulfillment of the requirements for the degree of Doctor of Philosophy in physics and allowed for defense by the Scientific Council of the Institute of Physics, University of Tartu.

Supervisors:

Prof. PhD.	Alvo Aabloo University of Tartu Tartu, Estonia
Prof. PhD.	Kwang J. Kim University of Nevada, Las Vegas Las Vegas, U.S.A.

Opponents:

Prof. PhD.	Barbar Akle Lebanese American University Byblos, Lebanon
Prof. PhD.	Mart Min Tallinn University of Technology Tallinn, Estonia

The public defense will take place on April 23rd, 2014 at 10:15 am in University of Tartu.

The publication of this dissertation was financed by Institute of Technology and Institute of Physics, University of Tartu.

Copyright: Deivid Pugal, 2014

ISSN 1406-0647
ISBN 978-9949-32-514-6(In print)
ISBN 978-9949-32-515-3(PDF)

University of Tartu Press
www.tyk.ee

Contents

List of original publications **8**

Author's contribution 8

Other publications 9

List of abbreviations **12**

1 Introduction **13**

1.1 IPMC research overview 13

1.1.1 Circuit equivalent models 17

1.1.2 Physics based models 18

1.2 Research motivation and contributions 19

2 Modeling method **24**

2.1 Adaptive *hp*-FEM 24

2.2 The Hermes library 25

2.3 Multimesh *hp*-FEM 26

3 *hp*-FEM model of Poisson-Nernst-Planck equations **29**

3.1 Model 29

3.1.1 Weak form of the PNP system 30

3.1.2 Jacobian matrix and residual vector for the Newton's method 32

3.1.3 Newton's iteration 34

3.2 Numerical Results and Comparisons 34
3.2.1 Comparison of single mesh low-order FEM and *hp*-FEM 37
3.2.2 Comparison of single-mesh and multi-mesh *hp*-FEM 38
3.2.3 Comparison of isotropic and anisotropic refinements 40
3.2.4 HP_ANISO adaptivity with physically more realistic boundary conditions 42
3.2.5 Length scale analysis 43
3.3 Chapter conclusions 46

4 *hp*-FEM model of IPMC deformation 47
4.1 Deformation model 47
4.1.1 Weak form of the equations 49
4.1.2 Jacobian matrix components and residual vector . . 50
4.2 Numeric results 51
4.2.1 Advantages of multi-mesh *hp*-FEM 52
4.2.2 Anisotropic refinements 53
4.2.3 Calculations with more advanced BCs 55
4.3 Chapter conclusions 60

5 Scalability and optimizations 61
5.1 Geometric scalability 61
5.2 PID time step control 65
5.3 Chapter conclusions 68

6 Conclusions 70

Bibliography 72

Acknowledgments 81

Summary in Estonian 82

Publications **85**

Curriculum Vitae **137**

Elulookirjeldus **138**

LIST OF ORIGINAL PUBLICATIONS

The current dissertation is based on the following original publications:

I D. Pugal, P. Solin, K. J. Kim, and A. Aabloo, "Modeling ionic polymer-metal composites with space-time adaptive multimesh *hp*-FEM," *Communications in Computational Physics*, vol. 11, no. 1, pp. 249–270, 2012.

II D. Pugal, P. Solin, K. Kim, and A. Aabloo, "*hp*-FEM electromechanical transduction model of ionic polymer–metal composites," *Journal of Computational and Applied Mathematics*, vol. 260, no. 0, pp. 135 – 148, 2014.

III D. Pugal, P. Solin, A. Aabloo, and K. J. Kim, "IPMC mechanoelectrical transduction: its scalability and optimization," *Smart Materials and Structures*, vol. 22, no. 12, p. 125029, 2013.

AUTHOR'S CONTRIBUTION

The publications that the dissertation is based on are a result of a collective effort with important contribution from all of the co-authors.

The author's contribution to the articles I–III were the research idea, majority of the derivation of the equations, equation implementation for Hermes, carrying out the simulations, and interpreting the results.

The author has also a number of related publications (IV–XXIX) that are not included in this dissertation, however, the research presented here is greatly inspired and affected by that work.

OTHER PUBLICATIONS ON THE RELATED FIELD

Books/dissertations:

IV D. Pugal, *Physics Based Model of Ionic Polymer-Metal Composite Electromechanical and Mechanoelectrical Transduction*. PhD thesis, University of Nevada, Reno, August 2012.

V K. J. Kim, X. Tan, H. R. Choi, and D. Pugal, *Biomimetic robotic artificial muscles*. World Scientific, 2013.

Articles:

IV C. Jo, D. Pugal, I.-K. Oh, K. J. Kim, and K. Asaka, "Recent advances in ionic polymer–metal composite actuators and their modeling and applications," *Progress in Polymer Science*, vol. 38, no. 7, pp. 1037 – 1066, 2013.

V V. Palmre, J. J. Hubbard, M. Fleming, D. Pugal, S. Kim, K. J. Kim, and K. K. Leang, "An IPMC-enabled bio-inspired bending/twisting fin for underwater applications," *Smart Materials and Structures*, vol. 22, no. 1, p. 014003, 2013.

VI J. Hubbard, M. Fleming, V. Palmre, D. Pugal, K. Kim, and K. Leang, "Monolithic IPMC fins for propulsion and maneuvering in bioinspired underwater robotics," *Oceanic Engineering, IEEE Journal of*, vol. PP, no. 99, pp. 1–12, 2013.

VII S. ik Son, D. Pugal, T. Hwang, H. R. Choi, J. C. Koo, Y. Lee, K. Kim, and J.-D. Nam, "Electromechanically driven variable-focus lens based on transparent dielectric elastomer," *Appl. Opt.*, vol. 51, pp. 2987–2996, May 2012.

VIII S. J. Kim, D. Pugal, W. Johnson, K. J. Kim, , and W. Yim, "A bio-inspired multi degree of freedom actuator based on a novel cylindrical ionic polymer-metal composite material," *Robotics and Autonomous Systems*, vol. 62, no. 1, pp. 53–60, 2012.

IX D. Pugal, K. J. Kim, and A. Aabloo, "An explicit physics-based model of ionic polymer-metal composite actuators," *Journal of Applied Physics*, vol. 110, no. 8, p. 084904, 2011.

X K. J. Kim, D. Pugal, and K. K. Leang, "A twistable ionic polymer-metal composite artificial muscle for marine applications," *Marine Technology Society Journal*, vol. 45, no. 4, pp. 83–98, 2011.

XI D. Pugal, K. Jung, A. Aabloo, and K. J. Kim, "Ionic polymer–metal composite mechanoelectrical transduction: review and perspectives," *Polymer International*, vol. 59, no. 3, pp. 279–289, 2010.

XII I.-S. Park, S.-M. Kim, D. Pugal, L. Huang, S.-W. Tam-Chang, and K. Kim, "Visualization of the cation migration in ionic polymer-metal composite under an electric field," *Applied Physics Letters*, vol. 96, no. 4, pp. 043301–043301–3, 2010.

XIII D. Pugal, K. J. Kim, A. Punning, H. Kasemagi, M. Kruusmaa, and A. Aabloo, "A self-oscillating ionic polymer-metal composite bending actuator," *Journal of Applied Physics*, vol. 103, no. 8, p. 084908, 2008.

XIV D. Kim, K. J. Kim, Y. Tak, D. Pugal, and I.-S. Park, "Self-oscillating electroactive polymer actuator," *Applied Physics Letters*, vol. 90, pp. 184104 –184104–3, 2007.

XV D. Pugal, A. Aabloo, and K. Kim, "Scalable low nDOF *hp*-FEM model of IPMC actuation," in *Proceedings of SPIE*, vol. 8687, pp. 86870X–86870X–10, 2013.

XVI V. Palmre, D. Pugal, K. K. Leang, and K. Kim, "The effects of electrode surface morphology on the actuation performance of IPMC," in *Proceedings of SPIE*, vol. 8687, pp. 86870W–86870W–10, 2013.

XVII D. Pugal, K. J. Kim, V. Palmre, K. K. Leang, and A. Aabloo, "Physics-based electromechanical model of IPMC considering various underlying currents," in *Proceedings of SPIE*, vol. 8340, pp. 83400P–83400P–10, 2012.

XVIII V. Palmre, D. Pugal, and K. Kim, "Characterization of longitudinal tensile force of millimeter thick IPMCs," in *Proceedings of SPIE*, vol. 8340, pp. 83402L–83402L–8, 2012.

XIX J. J. Hubbard, M. Fleming, K. K. Leang, V. Palmre, D. Pugal, and K. J. Kim, "Characterization of sectored-electrode IPMC-based propulsors for underwater locomotion," in *ASME Conference on Smart Materials, Adaptive Structures and Intelligent Systems (SMASIS)*, pp. 18–21, 2011.

XX S. Kim, D. Pugal, J. Wong, K. Kim, and W. Yim, "A bio-inspired multi degree of freedom actuator based on a novel cylindrical ionic polymer-metal composite material," in *Advanced Robotics (ICAR), 2011 15th International Conference on*, pp. 435–440, june 2011.

XXI D. Pugal, K. J. Kim, K. K. Leang, and V. Palmre, "Modeling and designing IPMCs for twisting motion: electromechanical and mechanoelectrical transduction," in *Proceedings of SPIE* (Y. Bar-Cohen and F. Carpi, eds.), vol. 7976, p. 79761S, 2011.

XXII D. Pugal, K. J. Kim, P. Solin, and A. Aabloo, "A novel *hp*-FEM model for IPMC actuation," in *Proceedings of SPIE*, vol. 7978, pp. 79780E–79780E–13, 2011.

XXIII S. J. Kim, D. Pugal, Y. Jung, J. Wong, K. J. Kim, and W. Yim, "A rod-shaped ionic polymer-metal composite for use as an active catheter-platform," *ASME Conference Proceedings*, vol. 2010, no. 44168, pp. 145–151, 2010.

XXIV D. Pugal, K. J. Kim, and A. Aabloo, "Modeling the transduction of IPMC in 3D configurations," in *Proceedings of SPIE*, vol. 7644, pp. 76441T–76441T–9, 2010.

XXV D. Pugal, S. J. Kim, K. J. Kim, and K. K. Leang, "IPMC: recent progress in modeling, manufacturing, and new applications," in *Proceedings of SPIE*, vol. 7642, pp. 76420U–76420U–10, 2010.

XXVI D. Pugal, A. Aabloo, K. J. Kim, and Y. Jung, "Modeling IPMC material with dynamic surface characteristics," in *ASME 2009 Conference on Smart Materials, Adaptive Structures and Intelligent Systems*, vol. 2, pp. 115–122, 2009.

XXVII D. Pugal, A. Aabloo, and K. J. Kim, "Dynamic surface resistance model of IPMC," in *Proceedings of SPIE* (Z. Ounaies and J. Li, eds.), vol. 7289, p. 72891E, 2009.

XXVIII D. Pugal, H. Kasemagi, M. Kruusmaa, and A. Aabloo, "An advanced finite element model of IPMC," in *Proceedings of SPIE* (Y. Bar-Cohen, ed.), vol. 6927, p. 692711, 2008.

XXIX D. Pugal, H. Kasemagi, K. J. Kim, M. Kruusmaa, and A. Aabloo, "Finite element simulations of the bending of the IPMC sheet," in *Proceedings of SPIE* (Y. Bar-Cohen, ed.), vol. 6524, p. 65240B, 2007.

List of Abbreviations

ANISO	Anisotropic
BC	Boundary condition
CDC	Carbide-derived-carbon
CPU	Central processing unit
DAP	Direct assembly process
DOF	Degrees of freedom
DPH	Distributed port-hamiltonian (system)
EAP	Electroactive polymer
FEM	Finite element method
IPMC	Ionic polymer-metal composite
ISO	Isotropic
LHS	Left hand side
PDE	Partial differential equation
PID	Proportional-Integral-Derivative
PNP	Poisson-Nernst-Planck
RHS	Right hand side
TBA	Tetra-n-butylammonium

CHAPTER 1

INTRODUCTION

Ionic polymer-metal composites (IPMC) have been studied during the past two decades for their potential to serve as noiseless mechanoelectrical and electromechanical transducers. The advantages of IPMC over other electroactive polymer actuators are low voltage bending, high strains ($> 1\%$), and an ability to work in wet environments. The main focus has been on the electromechanical transduction property – the material's ability to exhibit large bending deformation in response to a low (typically $1 \ldots 5$ V) applied voltage.

In order to describe both electromechanical and mechanoelectrical transduction properties of IPMC, an advanced physics based model of the material is necessary. In this dissertation, a fundamental physics based model that is based on novel *hp*-FEM (finite element method) is proposed. Full derivation of the equations with an in-depth study of the benefits of using higher order FEM with automatic adaptivity is presented.

The rest of the introduction chapter gives a thorough overview of IPMC materials, the latest models, and detailed research objectives of this dissertation.

1.1 IPMC research overview

IPMC consists of a thin ionomeric polymer membrane with thickness of upwards of 100 μm [1]. Typical membrane material is Nafion, however, other types of polymers such as Teflon and Flemion [2] are used as well. The membrane is coated with a thin layer of a noble metal electrode, such as platinum. Sometimes, an additional layer of gold is added on the surface

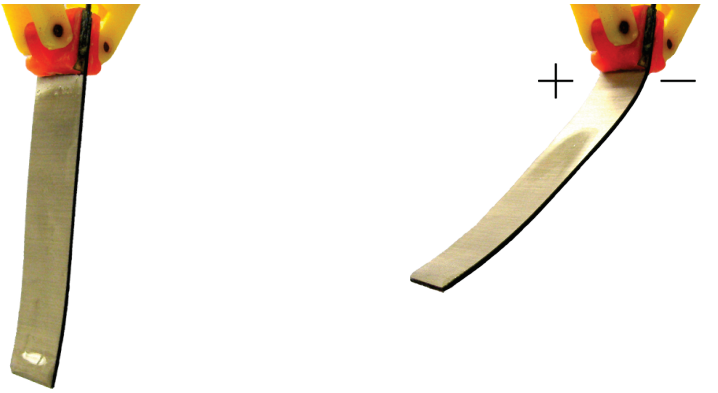

(a) (b)

Figure 1.1: IPMC electromechanical transduction in response to an applied voltage.

to improve the electric conductivity. The polymer membrane contains fixed anions and solvent with freely movable cations, so the overall charge of the material is balanced. Typical cations are Na^+, K^+, Li^+, and Cs^+ in water solution. Dry forms of IPMCs, where an ionic liquid is used instead of water based solvents have also been studied [3] (see Figure 1.1).

An IPMC actuator is shown in Figure 1.1 (a) and bending deformation in response to an applied voltage in Figure 1.1 (b). General conceptual design of IPMC was first described by Shahinpoor *et al.* in 1992 [4, 5]. In the following years, Segalman *et al.* also published a finite element analysis of the polymeric gel materials [6, 7]. Thereafter, attempts to formulate the electromechanical theory for IPMC materials were made. Shahinpoor and his co-workers presented a non-homogeneous large deformation theory of ionic polymer gels in electric and pH fields. The proposed model considers the spatial distribution of cations and anions inside the material due to the applied electric field. Deformation of IPMC was defined as a function of electric field strength, dimensions, and the material's physical parameters [8–10].

In 2000, De Gennes and his coworkers presented the first phenomenological theory of sensing and actuation of IPMC [11]; also, Nemat-Nasser and Li proposed a model of the electromechanical response of IPMC that considers the electrostatic forces inside the material and the cluster morphology of Nafion [12]. Soon after in 2002, Nemat-Nasser stressed the role of hydrated

cation transport within the clusters and polymeric networks of IPMC [13]. Few years later, Weiland and Leo published a model, where the rotation of individual dipoles within a cluster was studied and related to the actuation of IPMC [14]. In 2003, Nemat-Nasser presented an extensive study of actuation properties of IPMC with different membrane materials and cation types [2]. To summarize the study, typical Nafion based IPMC in most cation forms, when subjected to a small voltage, undergoes a fast bending towards the anode, followed by a slow relaxation towards the cathode. However, when some large alkyl-ammonium cations are being used (e.g TBA^+), the initial bending is rather gradual and the back relaxation is only partial. When subjected to a DC voltage, Nafion-based IPMCs generally do not maintain their initial displacement towards the anode and relax back towards the cathode. For some cations, the back relaxation goes even beyond the initial position [15, 16].

In the recent years, research of the IPMC materials has been mainly focused on getting higher efficiency, better adaptability to the environment, and applicability. Paquette and Kim investigated the low temperature behavior of IPMC and showed the material's capability to operate even below -20°C [17]. They also studied IPMC materials in a multilayer configuration and constructed an equivalent circuit model [18]. In 2006, Kim and Kim presented an electrochemical analysis of IPMC. They showed that the performance degradation of IPMC over time is possibly linked to Pt-oxide formation; they also suggested that the equivalent circuit of IPMC should include an inductive component to describe the actuation physics more accurately [19]. Later, they showed that the relaxation phenomena of the IPMC actuators are primarily caused by the overpotential of the surface electrodes and resulting platinum oxide formation [20]. In regard to IPMC's applicability, Anton analyzed the usability of the material for practical applications and demonstrated performance of IPMC using the inverted pendulum control [21]. He also published a detailed description of the quasi-static mechanical behavior of IPMC actuator at large deformation and showed that a short actuator with a rigid elongation behaves more linearly than a long one [22]. In 2007, Kim *et al.* showed that IPMC operation in a saltwater environment is feasible and naval applications could be considered [23]. In the same year, Dogruer *et al.* showed that, the hydrodynamic forces do not significantly affect the performance of the IPMC in aqueous environment and could be omitted from models [24]. In the following years, Kim and Kim conducted an extensive study of IPMC materials exhibiting self oscillations [25–27]. The physics behind the phenomenon is an electrochemical reaction on the Pt electrodes of IPMC that is im-

mersed in H_2SO_4 solution. A year later, Pugal *et al.* published a finite element model that couples actuation to the equations describing the oscillations [28, 29]. Recently, Dogruer *et al.* showed that IPMCs could be use for energy harvesting purposes. Shortly after, Tiwari studied IPMCs with different electrodes to understand the effectiveness of the energy harvesting process. Platinum IPMCs showed better charging in the bending and shear modes, whereas IPMCs with gold electrodes showed better battery charging in the extension mode [30]. A comprehensive research in regard to characterization of IPMCs for power harvesting was reported by Brufau-Penella *et al.* in 2008 [31] – a generic model that works with the IPMC material in dehydrated conditions was developed.

Conventional water solvent based IPMCs have also downsides – rather low efficiency, back-relaxation under DC voltage, electrode degradation over time, and water decomposition in the electrolysis reactions, to name a few [32]. To overcome some of these shortcomings, different polymer materials are being considered. For instance, some sulfonated polymers have high water uptake property, proton conductivity, ionic exchange capacity, and low cost [33–37]. Also, different electrode materials, manufacturing techniques, and more stable solvents have been studied. Akle *et al.* proposed a new manufacturing technique – Direct Assembly Process (DAP) – where an electrode material is sprayed onto ionic-liquid swollen Nafion and then hot-pressed [38]. In order to ensure large electrode surface area, Akle *et al.* used porous RuO_2 electrodes with ionic liquid 1-ethyl-3-methylimidazolium trifluoromethanesulfonate (EMITF) as solvent. The actuators showed good actuation performance and stability in air [39]. Fukushima and Asaka introduced a manufacturing technique to assemble bucky gel actuators – a dry actuator is fabricated layer-by-layer casting of bucky gel – a gelatinous room-temperature ionic liquid that contains single-walled carbon nanotubes (SWNTs). The actuator adopts a bimorph configuration with a polymer-supported internal ionic liquid electrolyte layer sandwiched by bucky-gel electrode layers. The advantage of the actuator is durability in air [40, 41]. Very quick response and large bending actuation was achieved by using 'super-growth' millimeter long SWNTs [42]. Palmre *et al.* introduced carbon aerogels [43] as a less expensive alternative material for assembling the EAP actuators [44]. Based on the same materials, Torop *et al.* proposed linear actuators capable of high force under low strain actuation [45]. Also, carbide-derived carbon (CDC) based electrodes have been studied as a simple, cost effective, yet very effective electrode material, that results high actuation strains [46, 47]. The CDC electrode based actuators with additional gold foil were demonstrated to have fast response under low actuation voltage [48].

A considerable effort has been put into modeling the physics of the electromechanical transduction of IPMC. One way to divide the models is by how the underlying physics is described. The first group is consists of rather empirical current-displacement relation models, often based on the electric circuit equivalent description. The second group of the models explicitly consider the ionic flux inside the material. Thus, both types of the models are based on the currents, however, the latter relates the calculated charge directly to the output deformation or force, whereas the former relates only the overall current (or applied voltage) to the tip displacement or couples the current to the torque in a mechanical beam.

1.1.1 Circuit equivalent models

Newbury and Leo developed an electric circuit model of IPMC. All the terms of the model are frequency dependent and a viscoelastic model is directly incorporated into the equations. The model provides means to analyze both actuation and sensing properties of the material [49]. Bonomo *et al.* introduced so-called grey box equivalent electric circuit model [50] that consists of two phases [51]. The first phase is to calculate the absorbed current based on the input voltage and the second is used to estimate either the blocking force or the tip displacement. Cabonetto *et al.* proposed a fractional order model using Marquardt method for the least squares estimation [52]. Brunetto *et al.* coupled the applied voltage to the stress in the IPMC and additionally considered the effect of viscous fluids (such as water) on the actuation performance of the material [53]. McDaid *et al.* developed a three-stage model that consists of equivalent electric circuit, electromechanical coupling term, and a mechanical actuation stage [54]. The model describes IPMC actuation response for various applied voltages up to 3 V. Punning *et al.* used the open-end transmission line presentation in order to model kinematics of IPMC in a linked manipulator application with IPMC based joints [55]. Interestingly, the work also suggests that using a rigid elongation instead of a long IPMC strip increases both efficiency and control precision. The detailed mathematical derivation of lossy RC distributed line model of IPMC was proposed by Punning and colleagues [56, 57].

Some models, however, consider both the electric circuit and also the underlying physics. For instance, Branco and Dente presented a continuum model of IPMC where a lumped-parametric circuit was derived to predict

relationship between applied voltage and current [58]. Rather novel approach was taken by Nishida *et al.* – they modeled IPMCs by using the distributed port-Hamiltonian (DPH) systems on multiple spatial scales [59]. The DPH systems represent systems of conservation laws in canonical way. More precisely, the system is described by *effort* and *flow* variables, called port variable pairs whose product has the dimension of power. The port variable pairs of the system can be used as boundary connections for various reduced models, e.g. numerical models with approximations such as electric circuit equivalent double layer, diffusion equations, and mechanical model.

1.1.2 Physics based models

The physics based models explicitly consider the ionic current in the polymer and relate calculated current or charge to the deformation of IPMC. Some models additionally include the physics of the electrodes. De Gennes introduced a transport model of ion and water molecules based on the linear irreversible thermodynamics [11]. Nemat-Nasser developed a comprehensive theory of IPMC actuation in 2000 [60] and further improved it in 2002 [13] – he used fundamental equations to describe the ionic current, induced forces in Nafion clusters, and corresponding bending of IPMC. Asaka and Oguro developed a model based on electro-osmotic flow and pressure driven water flux description also in 2000 [61].

More recently, Porfiri studied the charge dynamics and capacitance of IPMC [62]. He proposed an analytical solution to the initial value problem based on matched asymptotic expansions; thereafter, based on the analytical model, a circuit model of IPMC was derived. Capacitance dependence on the applied voltage was also discussed. Chen and Tan used somewhat similar approach to develop a control design for IPMC – they solved the physics-governed partial differential equation (PDE) based model in the Laplace domain and incorporated it in a control design by using model reduction [63]. Wallmersperger *et al.* showed that the large surface area effect of the electrode can be incorporated in the ion transport model by significantly increasing dielectric permittivity value and diffusion constant in respective equations [64]. This helps to avoid calculating highly nonlinear and very steep cation concentration and electric potential gradients near the polymer boundaries – challenging to model with FEM. Akle *et al.* studied both numerically and experimentally high surface area effect on the induced current and showed that higher electrode surface area results in more stored charge and also different charge accumulation dynamics [65].

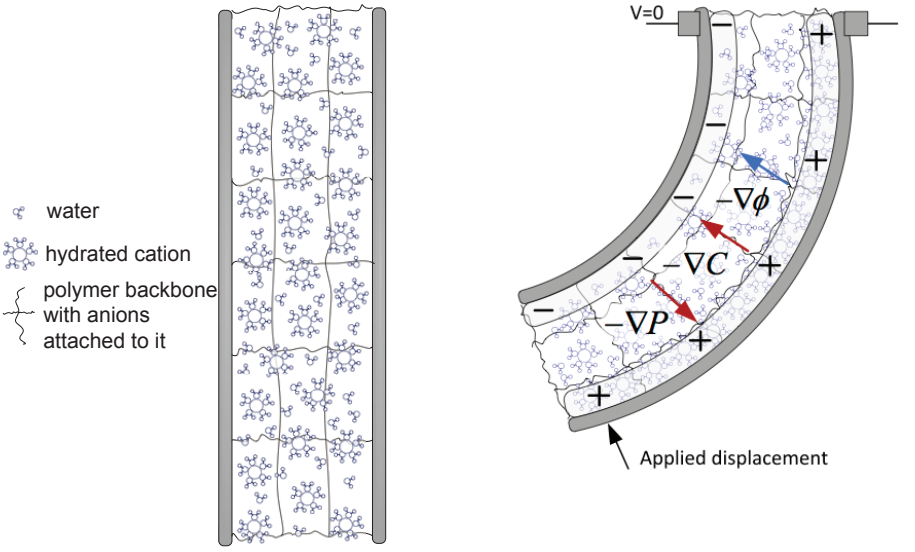

(a) (b)

Figure 1.2: IPMC model consisting of solvent (water) with hydrated cations and polymer backbone with anions (a); deformation induced mechanoelectrical transduction with cation concentration C, electric potential ϕ and pressure P field gradients (b).

1.2 Research motivation and contributions

Ongoing research on the electromechanical and mechanoelectrical transduction of IPMC materials has been focused on thorough understanding of the underlying physics. The model of mechanoelectrical transduction is illustrated in Figure 1.2. More precisely, from the fundamental aspect, a physics based model has been derived that is based on the boundary conditions that can be easily measured and applied to reduce the number of unknown parameters. From the mathematical aspect, various methods were actively researched to model the equations efficiently. This dissertation focuses mainly on the mathematical aspect. After introducing the model, it will be demonstrated in detail how a novel *hp*-FEM method can be applied in modeling the phenomenon.

The physics based modeling of IPMC transduction can be divided into two different problems: modeling the ionic flux inside the polymer and modeling the deformation in response to the ionic flux or as a cause of the flux.

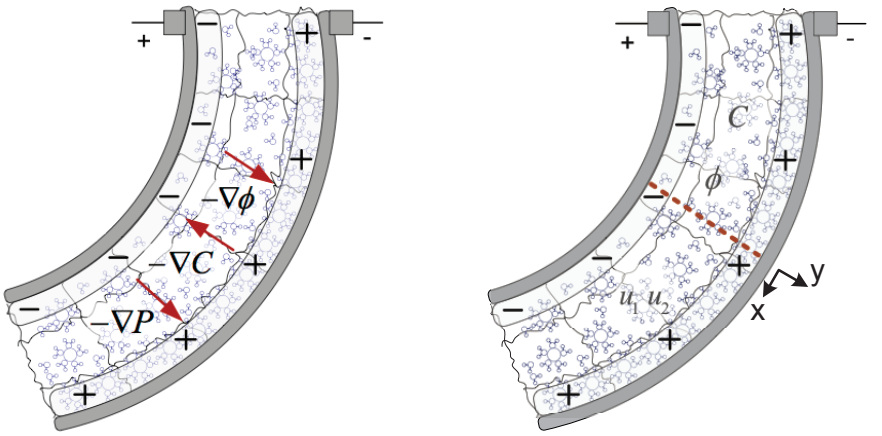

(a) (b)

Figure 1.3: IPMC electromechanical transduction modeled with cation concentration C, electric potential ϕ and pressure P field gradients. (a); optimized model with calculated variables C and ϕ with x-directional displacement u_1 and y-directional displacement u_2 (b).

The ionic flux is calculated by solvent the system of Poisson-Nernst-Planck equations (further abbreviated PNP); the optimized Nernst-Planck equation for the mobile cations has the form

$$\frac{\partial C}{\partial t} + \nabla \cdot (-D\nabla C - \mu F C \nabla \phi) = 0, \tag{1.1}$$

where C stands for cation concentration with the initial value of C_0, D is diffusion constant, μ mobility, F Faraday constant, and ϕ voltage. The Poisson equation has the form

$$-\nabla^2 \phi = \frac{F\rho}{\varepsilon} \tag{1.2}$$

where ε is the absolute dielectric permittivity. The charge density $\rho = C - C_0$ where C_0 is a constant anion concentration. Deformation can be expressed by using the Navier's equation in the vector form [66]

$$(\lambda + \mu)\, u_{k,ki} + \mu u_{i,jj} + F_i = 0, \tag{1.3}$$

where u_i is a component of the displacement vector, F_i body force, and λ and μ are Lame's constants. The model with all the variables is illustrated in Figure 1.3.

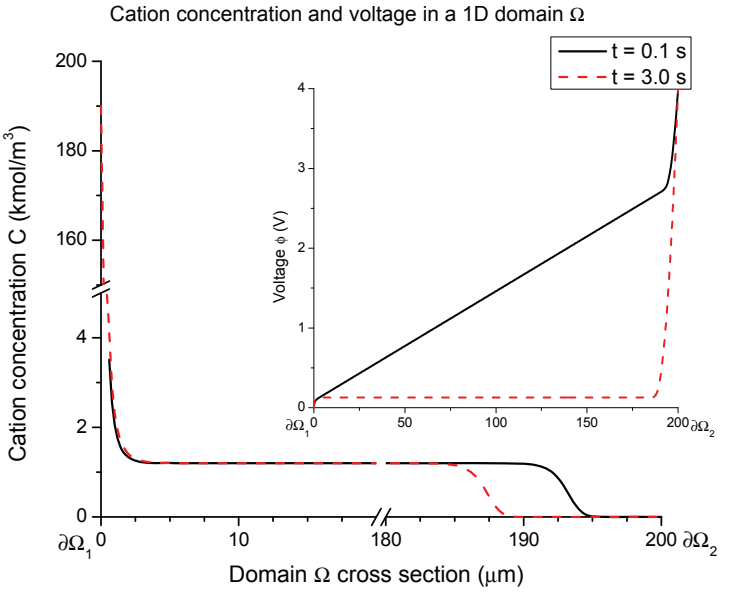

Figure 1.4: Sample concentration C and voltage ϕ in a 1D domain $\Omega \subset \mathbb{R}$. Dirichlet boundary conditions ($V_{\partial\Omega_1} = 0$ V and $V_{\partial\Omega_2} = 4$ V) were applied to the Poisson equation (1.2) and Neumann conditions to the Nernst-Planck equation (1.1).

The ionic flux calculated with (1.1), (1.2) and deformation (1.3) can be solved as decoupled in many optimized cases [28, 29, 67], however, this can result in loss of overall calculation precision and complicate the simulation procedure [68]. Regardless of the approach, solving for the variables imposes a number of challenges on the model and a solution method.

Figure 1.4 depicts a solution for the fields C and ϕ at $t = 0.1$ s and $t = 3.0$ s in a cross-section of IPMC (denoted by the dashed line in Figure 1.3 (b)). It can be observed that the solution has two notable characteristics: for the most part of the calculation domain (denoted by Ω), the gradient $\nabla C = 0$. Close to $\partial\Omega_2$, ∇C is nonzero and moving in time, and ∇C is very large at $\partial\Omega_1$. At the same time, ϕ is a "nice" smooth function for the most part of Ω but it has a large gradient at $\partial\Omega_2$. Additionally, the displacement fields u_1 and u_2 are rather smooth functions in the entire domain of Ω as illustrated in Figure 1.5. The nature of the problem makes the choice of an optimal mesh highly problematic. When a chosen mesh is too coarse, solution CPU (central processing unit) time and memory are lower, however, the approximation error of the solution can be high. When a too fine mesh

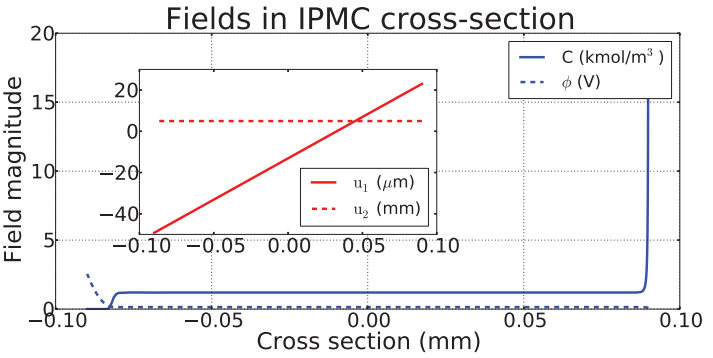

Figure 1.5: Calculated C and ϕ (on the main graph), u_1 and u_2 (on the subgraph) in IPMC cross-section (see Figure 1.3 (b)).

is chosen, the relative error is reduced, however, CPU time and memory usage could become overly high, especially if the problem is solved in a 3D domain. In fact, it has been shown that the computing power required for a full scale problem is significant [69].

The challenge is to optimize the solution for CPU time and required memory, while maintaining a prescribed maximum relative error. Even if the solution shown in Figure 1.4 was a stationary, an optimal mesh for C could never be optimal for ϕ and vice versa. Considering also the transient nature of the solution, it is not possible to find a mesh that would be suitable for each calculation step while maintaing a prescribed precision when using the conventional FEM. Furthermore, the shape of the solution in Figure 1.4 suggests that besides optimizing the size of the elements of the mesh, the polynomial degree of finite elements in the middle of the domain Ω and near the boundaries $\partial\Omega_1$, $\partial\Omega_2$ should be different — large low-degree elements should be used in the middle of the domain while small higher degree ones should be used in the boundary layers.

In this dissertation, a comprehensive study of solving PNP and PNP-Navier's system of equation using adaptive algorithms is presented. First, the explicit weak-form of the PNP system for Newton's method is presented. Thereafter, a brief overview of a novel adaptive multi-mesh *hp*-FEM is introduced and the residual vector and Jacobian matrix of the system is derived and implemented using *hp*-FEM library Hermes. It is shown how such problem benefits from using individual meshes with mutually independent adaptivity mechanisms. To begin with, a model consisting of only the PNP system is solved using different adaptivity algorithms. For instance, it is demonstrated that the PNP problem with set of constants that results

Debye's length in nanometer scale can be successfully solved. Based on those results, the complete PNP-Navier's system of equations is studied. It is shown how *hp*-FEM helps to keep the problem geometrically scalable. Additionally, it is shown how employing a PID controller based time step adaptivity helps to reduce the calculation time.

The outline of the work is as follows. The modeling method is explained in Chapter 2 (article I). The comprehensive study of *hp*-FEM calculations of the PNP system of equations is presented in Chapter 3 (article I). Thereafter, IPMC deformation is model (the PNP-Navier's system of equations) is studied in Chapter 4 (article II). Finally, some possible optimizations for solving the problem more efficiently are explored in Chapter 5 (articles I and III). The work is concluded in Chapter 6.

CHAPTER 2

MODELING METHOD

The *hp*-FEM is a modern version of the finite element method (FEM) that attains very fast convergence rates by combining optimally finite elements of variable size (h) and polynomial degree (p) [70, 71]. The main principles of exponential convergence are that very smooth, polynomial-like functions are approximated using large high-order elements and non-analytic functions such as singularities are approximated via small low-order ones. The superiority of the *hp*-FEM over standard (low-order) FEM has been demonstrated, for instance, by [72–74]. Although the implementation of the *hp*-FEM is involved, the method is becoming increasingly popular. An overview of the method and comparison with the traditional FEM is provided in this chapter.

2.1 Adaptive *hp*-FEM

The *hp*-FEM is a modern version of the finite element method that is capable of exponential convergence (the approximation error drops exponentially as new degrees of freedom are added during adaptivity) while standard FEM can only attain algebraic (polynomial) convergence rates which are much slower [70].

In traditional low-order FEM (based on piecewise-linear or piecewise quadratic elements), refining an element is not algorithmically complicated, and so the most difficult part is to find out what elements should be refined. To do this, various techniques ranging from rigorous guaranteed a-posteriori

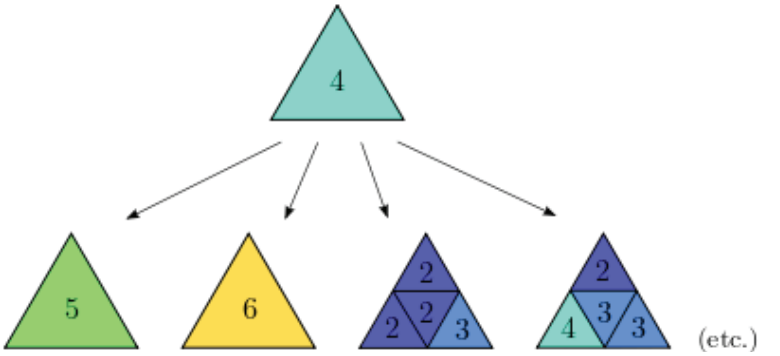

Figure 2.1: Many possible refinement candidates for a fourth-order element.

error estimates to heuristic criteria such as residual error indicators or error indicators based on steep gradients are employed.

However, these approaches are in general not very well suited for multi-physics coupled problems or higher-order finite element methods: Rigorous guaranteed error estimates only exist for very simple problems (such as linear elliptic PDE) and only for low-order finite elements. Heuristic techniques are usually somehow doable for all problems, but they fail in more complicated situations. Moreover, they lack a transparent relation to the true approximation error and thus they may give wrong results.

Automatic adaptivity in higher-order finite element methods (*hp*-FEM) is much different from adaptivity in low-order FEM. Firstly, analytical error estimates capable of guiding adaptive *hp*-FEM do not exist even for the simplest linear elliptic equations, not speaking about nonlinear multiphysics coupled systems. Secondly, a higher-order element can be refined in many different ways, as illustrated in Figure 2.1.

The number of possible element refinements is implementation dependent. In general it is very low in *h*-adaptivity and *p*-adaptivity, and much higher in *hp*-adaptivity. Moreover, this number grows very fast when anisotropic refinements are enabled.

2.2 The Hermes library

Hermes[1] is a free and open-source C++ library that implements higher-order finite elements approximations and adaptive *hp*-FEM. It supports

[1] http://hpfem.org/hermes

8 different adaptivity modes – three isotropic and five anisotropic. The isotropic refinements are h-isotropic (H_ISO), p-isotropic (P_ISO), hp-isotropic (HP_ISO). Anisotropic refinement modes are h-anisotropic (H_ANISO), hp-anisotropic-h (HP_ANISO_H), p-anisotropic (P_ANISO), hp-anisotropic-p (HP_ANISO_P), and hp-anisotropic (HP_ANISO). The eight adaptivity modes are summarized in Figure 2.2. It must be noted that in case of HP_ANISO_H, only element size is adapted anisotropically whereas polynomial degree is adapted isotropically. The opposite holds true for HP_ANISO_P.

Note that triangular elements do not support anisotropic refinements. Due to the large number of refinement options, classical error estimators that provide a constant error estimate per element, cannot be used to guide automatic hp-adaptivity. For this, one needs to know the shape of the approximation error. Hermes uses a pair of approximations with different orders of accuracy to obtain this information: coarse mesh solution and fine mesh solution [75]. The initial coarse mesh is read from the mesh file, and the initial fine mesh is created through its global refinement both in h and p. The fine mesh solution is the approximation of interest both during the adaptive process and at the end of computation. Global orthogonal projection of the fine mesh solution on the coarse mesh is used to extract the low-order part from the reference solution. The adaptivity algorithm is guided by the difference between the reference solution and its low-order part. Note that this approach to automatic adaptivity is PDE-independent and thus naturally applicable to a large variety of multiphysics coupled problems.

2.3 Multimesh *hp*-FEM

In multiphysics PDE systems such as Poisson-Nernst-Planck it can happen that one physical field is very smooth where others are not, as it was illustrated in Figure 1.4. If all the fields are approximated on the same mesh, then unnecessary refinements will be present in smooth areas where they are not necessary. This can be very wasteful.

Hermes implements a novel adaptive multimesh hp-FEM [76–78] that makes it possible to approximate different fields on individual meshes, without breaking the monolithic structure of the coupling mechanism. For practical reasons, the meshes in the system are not allowed to be completely independent – they have a common coarse mesh that is called *master mesh*. The master mesh is there for algorithmic purposes only and it may not even

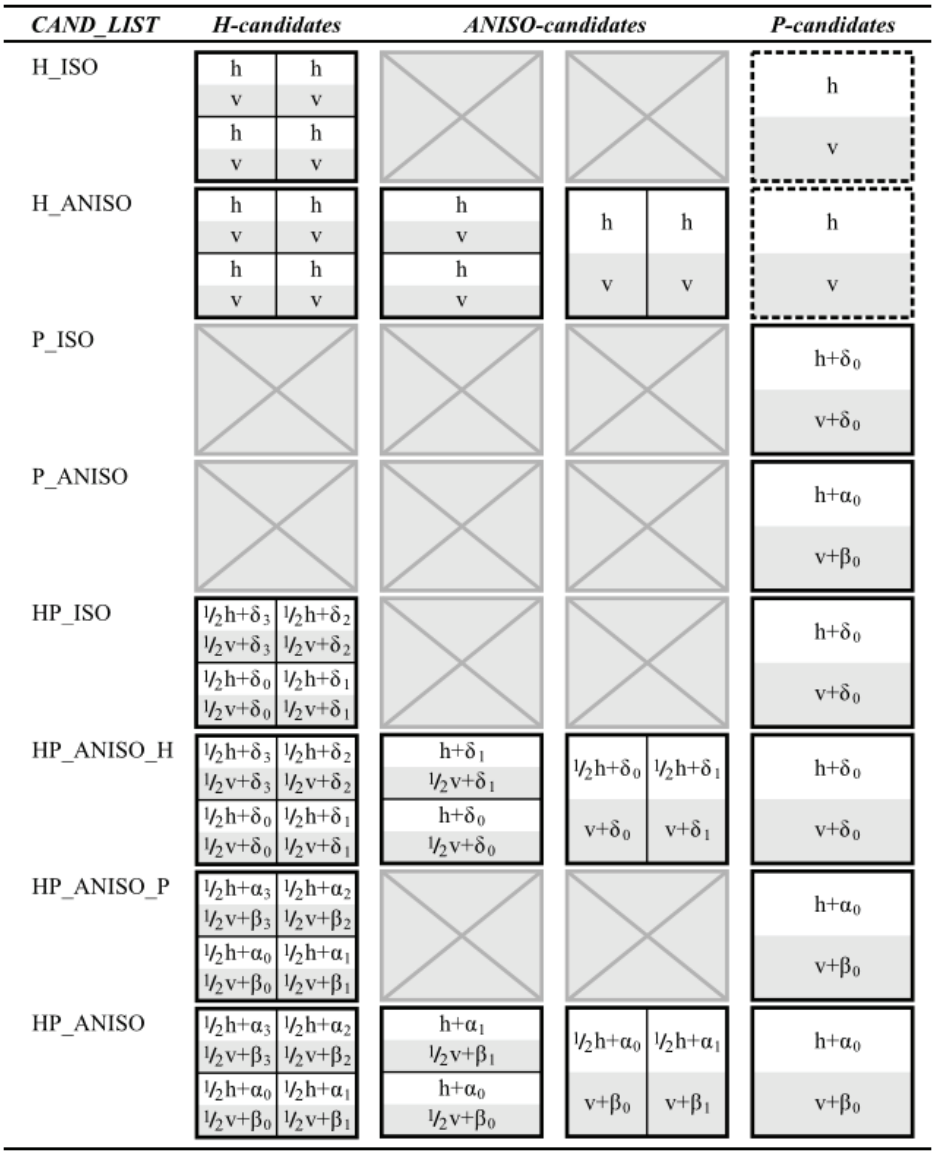

Figure 2.2: Refinement candidates for every refinement mode for quad type elements.

be used for discretization purposes. Every mesh in the system is obtained from the master mesh via an arbitrary sequence of elementary refinements. Assembling is done on a *union mesh*, a geometrical union of all meshes in the system (imagine printing all meshes on transparencies and positioning them on top of each other).

The union mesh is not constructed physically in the computer memory – it merely serves as a hint to correctly transform the integration points while integrating over sub-elements of elements in the existing meshes. As a result, the multimesh discretization of the PDE system is monolithic in the sense that no physics is lost — all integrals in the discrete weak formulations are evaluated exactly up to the error in the numerical quadrature. The exact preservation of the coupling structure of multiphysics coupled problems makes the multimesh *hp*-FEM very different from various interpolation and projection based methods that suffer from errors made while transferring data between different meshes in the system.

CHAPTER 3

hp-FEM MODEL OF POISSON-NERNST-PLANCK EQUATIONS

In this chapter, Poisson-Nernst-Planck (PNP) system of equations is modeled using *hp*-FEM. The system of equation is used to calculate charge transport in IPMC material. To make the results easily reproducible, complete mathematical basis of the model with detailed derivation is presented. In order to find the best adaptive mode for this type of coupled problem, a large numerous computations were performed using various adaptivity modes in single-mesh and multi-mesh configurations. A number of these comparative calculation results will be presented.

3.1 Model

A rectangular 2D domain $\Omega \subset \mathbb{R}^2$ with boundaries $\partial\Omega_{1...4} \subset \partial\Omega$, shown in Figure 3.1 is considered. The domain presents the cross-section of IPMC. As there is no flow through the domain's boundary, Eq. (1.1) is equipped with a Neumann boundary condition

$$- D\frac{\partial C}{\partial n} - \mu FC\frac{\partial \phi}{\partial n} = 0. \tag{3.1}$$

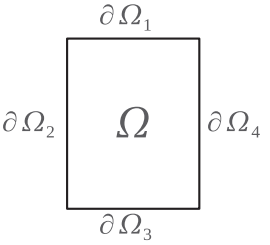

Figure 3.1: Calculation domain $\Omega \subset \mathbb{R}^2$ with boundaries $\partial\Omega_{1\ldots4} \subset \partial\Omega$.

Furthermore, a positive constant voltage V_{pos} is prescribed on Ω_1 and zero voltage on Ω_3:

$$\phi_{\partial\Omega_1} = V_{pos}, \tag{3.2}$$
$$\phi_{\partial\Omega_3} = 0. \tag{3.3}$$

On the rest of the boundary, ϕ has zero normal derivatives, and thus a Neumann boundary condition is prescribed

$$\frac{\partial\phi_{\Omega_2}}{\partial n} = \frac{\partial\phi_{\Omega_4}}{\partial n} = 0. \tag{3.4}$$

3.1.1 Weak form of the PNP system

In the following, derivation of weak forms of Eqs. (1.1) and (1.2), as well as formulas for the Jacobian matrix and residual vector that are used in actual computations are derived. To simplify notation, a dimensionless formulation of Eqs. (1.1) and (1.2) will be used in calculations. The following new notations for the independent variables x, y, t and for the dependent variables C and ϕ are used [79]:

$$X = \frac{x}{l}, \quad Y = \frac{y}{l}, \quad \tau = \frac{tD}{\lambda_D l}, \quad \varphi = \frac{\phi F}{RT}, \quad c = \frac{C}{C_0}. \tag{3.5}$$

Here λ_D is the Debye screening length and it is expressed as follows [79]:

$$\lambda_D = \sqrt{\frac{\varepsilon RT}{2F^2 C_0}}. \tag{3.6}$$

After inserting variables (3.5) into Eq. (1.1) the Nernst-Planck equation and Poisson equation become:

$$\frac{DC_0}{\lambda_D l}\frac{\partial c}{\partial \tau} + \frac{1}{l}\nabla_d \cdot \left(-\frac{DC_0}{l}\nabla_d c - c\frac{DC_0}{l}\nabla_d \varphi \right) = 0 \tag{3.7}$$

$$-\frac{\varepsilon RT}{l^2 F^2 C_0}\nabla_d^2 \varphi = c - 1, \tag{3.8}$$

where

$$\nabla_d = \left(\frac{\partial}{\partial X}, \frac{\partial}{\partial Y} \right). \tag{3.9}$$

After simplifying Eqs. (3.7) and (3.8) and denoting

$$\epsilon = \frac{\lambda_D}{l}, \tag{3.10}$$

the dimensionless form of the PNP system of equations becomes

$$\frac{\partial c}{\partial \tau} - \epsilon \nabla_d^2 c - \epsilon \nabla_d \cdot (c \nabla_d \varphi) = 0, \tag{3.11}$$

$$-\nabla_d^2 \varphi = \frac{c-1}{2\epsilon^2}. \tag{3.12}$$

Boundary condition Eq. (3.1) has the form

$$-\frac{\partial c}{\partial n} - c\frac{\partial \varphi}{\partial n} = 0. \tag{3.13}$$

As the second derivatives of both c and φ are present in the equations, the appropriate function space for them is the Sobolev space $V = H^1(\Omega)$ where

$$H^1(\Omega) = \left\{ v \in L^2(\Omega);\ \nabla_d v \in \left[L^2(\Omega) \right]^2 \right\}.$$

In order to derive the weak form of the Nernst-Planck equation, Eq. (3.11) is first multiplied with a test function $v^c \in V$ and integrated over the domain Ω,

$$\int_\Omega \frac{\partial c}{\partial \tau} v^c d\mathbf{x} - \int_\Omega \epsilon \nabla_d^2 c v^c d\mathbf{x} - \int_\Omega \epsilon \nabla_d c \cdot \nabla_d \varphi v^c d\mathbf{x} - \int_\Omega \epsilon c \nabla_d^2 \varphi v^c d\mathbf{x} = 0. \tag{3.14}$$

Thereafter, the Green's first identity is applied to the terms that contain second derivatives

$$\int_\Omega \frac{\partial c}{\partial \tau} v^c d\mathbf{x} + \epsilon \int_\Omega \nabla_d c \cdot \nabla_d v^c d\mathbf{x} - \epsilon \int_\Omega \nabla_d c \cdot \nabla_d \varphi v^c d\mathbf{x}$$

$$+\epsilon\int_\Omega \nabla_d\left(cv^c\right)\cdot\nabla_d\varphi d\mathbf{x}-\epsilon\int_{\partial\Omega}\frac{\partial c}{\partial n}v^c d\mathbf{S}-\int_{\partial\Omega}\epsilon\frac{\partial\varphi}{\partial n}cv^c d\mathbf{S}=0. \quad (3.15)$$

Expanding the nonlinear term and using the boundary condition (3.13) results in

$$\int_\Omega\frac{\partial c}{\partial\tau}v^c d\mathbf{x}+\epsilon\int_\Omega\nabla_d c\cdot\nabla_d v^c d\mathbf{x}-\epsilon\int_\Omega\nabla_d c\cdot\nabla_d\varphi v^c d\mathbf{x}$$

$$+\epsilon\int_\Omega\nabla_d\varphi\cdot\nabla_d cv^c d\mathbf{x}+\epsilon\int_\Omega c\left(\nabla_d\varphi\cdot\nabla_d v^c\right)d\mathbf{x}=0. \quad (3.16)$$

After the third and fourth terms cancel out, the final weak form of the Nernst-Planck equation is obtained

$$\int_\Omega\frac{\partial c}{\partial\tau}v^c d\mathbf{x}+\epsilon\int_\Omega\nabla_d c\cdot\nabla_d v^c d\mathbf{x}+\epsilon\int_\Omega c\left(\nabla_d\varphi\cdot\nabla_d v^c\right)d\mathbf{x}=0. \quad (3.17)$$

Analogously, the weak form of the Poisson equation (3.12) is also derived

$$-\int_\Omega\nabla_d^2\varphi v^\varphi d\mathbf{x}-\frac{1}{2\epsilon^2}\left[\int_\Omega cv^\varphi d\mathbf{x}-\int_\Omega v^\varphi d\mathbf{x}\right]=0. \quad (3.18)$$

After performing integration by parts and taking into account the boundary conditions for φ, the final weak form of Poisson equation is

$$\int_\Omega\nabla_d\varphi\cdot\nabla_d v^\varphi d\mathbf{x}-\frac{1}{2\epsilon^2}\left[\int_\Omega cv^\varphi d\mathbf{x}-\int_\Omega v^\varphi d\mathbf{x}\right]=0. \quad (3.19)$$

3.1.2 Jacobian matrix and residual vector for the Newton's method

To employ the Newton's method for the nonlinear system (3.17), (3.19), formulas for the Jacobian matrix and residual vector need to be derived. Time discretization will be performed using the second-order Crank-Nicolson method. The unknown solution components c^{n+1} and φ^{n+1} at the end of the time step $\delta\tau$ are expressed as linear combinations of finite element basis functions v_k^c and v_k^φ with unknown coefficients,

$$c^{n+1}=c(Y^{n+1}) \;=\; \sum_{k=1}^{N^c}y_k^c v_k^c, \quad (3.20)$$

$$\varphi^{n+1}=\varphi(Y^{n+1}) \;=\; \sum_{k=1}^{N^\varphi}y_k^\varphi v_k^\varphi. \quad (3.21)$$

Here Y^{n+1} is a coefficient vector of length N^c+N^φ comprising the unknown solution coefficients y_k^c and y_k^φ (in this order). We will also be using $c^n = c(Y^n)$ and $\varphi^n = \varphi(Y^n)$ for the previous time step solutions.

With the notation (3.20), (3.21), the time discretized Eq. (3.17) leads to the formula for the first part F^c of the residual vector F,

$$\begin{aligned} F_i^c(Y) &= \int_\Omega \frac{c(Y)}{\delta\tau} v_i^c d\mathbf{x} - \int_\Omega \frac{c^n}{\delta\tau} v_i^c d\mathbf{x} \\ &\quad + \frac{1}{2}\epsilon \left[\int_\Omega \nabla_d c(Y) \cdot \nabla_d v_i^c d\mathbf{x} + \int_\Omega \nabla_d c^n \cdot \nabla_d v_i^c d\mathbf{x} \right. \\ &\quad + \int_\Omega c(Y) \left(\nabla_d \varphi(Y) \cdot \nabla_d v_i^c \right) d\mathbf{x} \\ &\quad \left. + \int_\Omega c^n \left(\nabla_d \varphi^n \cdot \nabla_d v_i^c \right) d\mathbf{x} \right. \end{aligned} \tag{3.22}$$

where $i = 1, 2, \ldots, N^c$. Analogously, Eq. (3.19) defines the second part F^φ of the residual vector F,

$$F_i^\varphi(Y) = \int_\Omega \nabla_d \varphi(Y) \cdot \nabla_d v_i^\varphi d\mathbf{x} - \frac{1}{2\epsilon^2} \left[\int_\Omega c(Y) v_i^\varphi d\mathbf{x} - \int_\Omega v_i^\varphi d\mathbf{x} \right] \tag{3.23}$$

where $i = N^c+1, N^c+2, \ldots, N^c+N^\varphi$. The nonlinear discrete problem that needs to be solved at the end of each time step thus has the form $F(Y) = 0$.

The Jacobian matrix $J(Y) = DF/DY$ has a 2×2 block structure,

$$J(Y) = \begin{pmatrix} \dfrac{\partial F_i^c}{\partial y_j^c} & \dfrac{\partial F_i^c}{\partial y_j^\varphi} \\ \dfrac{\partial F_i^\varphi}{\partial y_j^c} & \dfrac{\partial F_i^\varphi}{\partial y_j^\varphi} \end{pmatrix}, \tag{3.24}$$

and its entries are obtained by calculating the partial derivatives of F with respect to the components of the coefficient vector Y. For this it is useful to realize that

$$\frac{\partial c(Y)}{\partial y_j^c} = v_j^c, \quad \frac{\partial \nabla_d c(Y)}{\partial y_j^c} = \nabla_d v_j^c, \quad \text{etc..}$$

The components of the Jacobian matrix are obtained as follows:

$$\begin{aligned}
\frac{\partial F_i^c}{\partial y_j^c}(Y) &= \int_\Omega \frac{1}{\delta\tau} v_j^c v_i^c d\mathbf{x} + \frac{1}{2}\epsilon \int_\Omega \nabla_d v_j^c \cdot \nabla_d v_i^c d\mathbf{x} \\
&\quad + \frac{1}{2}\epsilon \int_\Omega v_j^c \left(\nabla_d \varphi(Y) \cdot \nabla_d v_i^c\right) d\mathbf{x}, \qquad (3.25) \\
\frac{\partial F_i^c}{\partial y_j^\varphi}(Y) &= \frac{1}{2}\epsilon \int_\Omega c(Y) \left(\nabla_d v_j^\varphi \cdot \nabla_d v_i^c\right) d\mathbf{x}, \qquad (3.26) \\
\frac{\partial F_i^\varphi}{\partial y_j^c}(Y) &= -\frac{1}{2\epsilon^2} \int_\Omega v_j^c v_i^\varphi d\mathbf{x}, \qquad (3.27) \\
\frac{\partial F_i^\varphi}{\partial y_j^\varphi}(Y) &= \int_\Omega \nabla_d v_j^\varphi \cdot \nabla_d v_i^\varphi d\mathbf{x}. \qquad (3.28)
\end{aligned}$$

3.1.3 Newton's iteration

At the beginning of the $(n+1)$st time step Y_0^{n+1} is set to $Y_0^{n+1} = Y^n$, where Y^n is the coefficient vector that was calculated in the nth time step (or coming from the initial condition if $n = 0$). We set $k = 0$ and run the Newton's iteration

$$\begin{aligned}
J(Y_k^{n+1})\delta\tau Y_{k+1}^{n+1} &= -F(Y_k^{n+1}), \\
Y_{k+1}^{n+1} &= Y_k^{n+1} + \delta\tau Y_{k+1}^{n+1}, \\
k &:= k+1
\end{aligned}$$

over k until it converges. Then we set $Y^{n+1} := Y_k^{n+1}$. A combined stopping criterion is used to make sure that both the norm of the residual vector $\|F(Y^{n+1})\|$ as well as the norm of the increment $\|\delta Y^{n+1}\|$ are sufficiently small.

3.2 Numerical Results and Comparisons

The solutions to the PNP problem exhibit a specific behavior that was described in Chapter 1. In order to find the best adaptive method to deal with this type of problems, a large number of computations were performed using all adaptivity modes in both the single-mesh and multi-mesh regimes. In the numerical experiments attention was paid to the relative error, cumulative CPU time, and problem size in terms of number of degrees of freedom (DOF) in each time step. The scaled variables c and φ and the

unscaled time t are used to present the solutions. The simulations were performed with physical time step of 0.05 s and the final time of 3.0 s was chosen as it is close to the time scaling constant τ. The time step was chosen after many numerical experiments in such a way that the error in time was approximately the same as the error in space. The implementation of advanced adaptive implicit higher-order Runge-Kutta methods is part of future work.

Two types of initial meshes were used — a finer mesh shown in Figure 3.2 (b) was used for p-adaptivity and a very coarse initial mesh shown in Figure 3.2 (a) was used for h-adaptivity and hp-adaptivity. The constants used in the calculations are shown in Table 3.1.

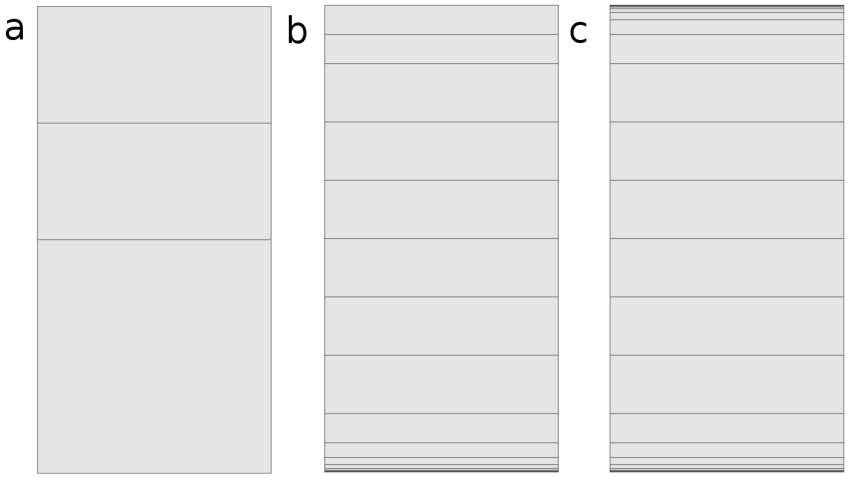

Figure 3.2: Initial coarse mesh (a), refined mesh (b), and symmetrically refined mesh for length scale study (c). The coarse mesh (a) and refined mesh (b) were used in the initial calculations, the latter one in case of p-adaptivity (including HP_ANISO_P).

An example of the solution at $t = 0.1$ s and $t = 3.0$ s calculated with the HP_ANISO refinement mode is shown in Figures 3.3 and 3.4.

It can be seen that at $t = 0.1$ s some ionic migration has already taken place and large concentration gradients near the boundaries $\partial\Omega_1$ and $\partial\Omega_3$ have formed. The figures also show that the meshes at $t = 0.1$ s and $t = 3.0$ s are different.

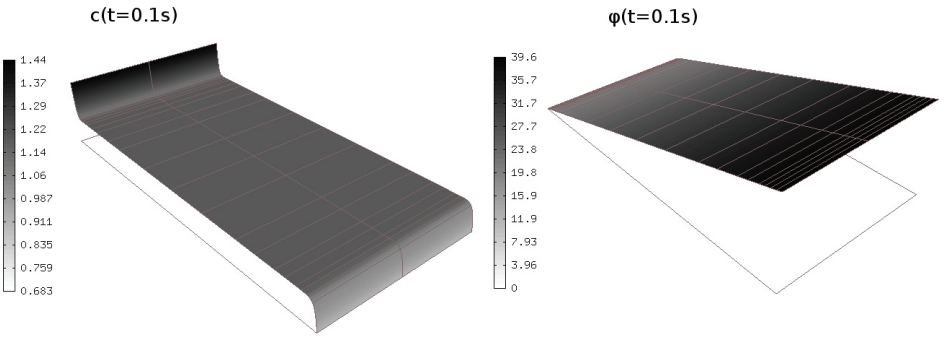

Figure 3.3: Scaled concentration c and voltage φ at $t = 0.1\ s$.

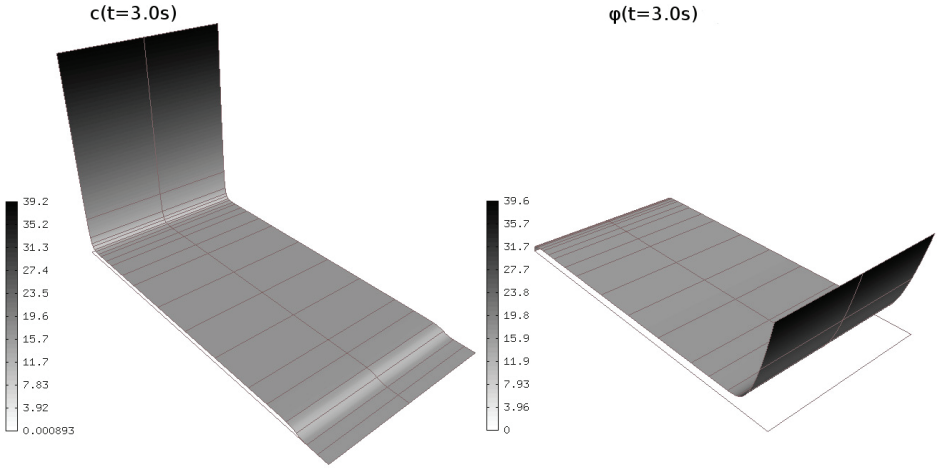

Figure 3.4: Scaled concentration c and voltage φ at $t = 3.0\ s$.

Table 3.1: Constants used in the PNP system of equations.

Constant	Value	Unit	Description
D	10×10^{-11}	$\frac{\mathrm{m}^2}{\mathrm{s}}$	Diffusion constant
z	1	-	Charge number
F	96,485	$\frac{\mathrm{C}}{\mathrm{mol}}$	Faraday number
R	8.31	$\frac{\mathrm{J}}{\mathrm{mol \cdot K}}$	The gas constant
$\mu\ \left(= \frac{D}{RT}\right)$	4.11×10^{-14}	$\frac{\mathrm{mol \cdot s}}{\mathrm{kg}}$	Electrical mobility
C_0	1,200	$\frac{\mathrm{mol}}{\mathrm{m}^3}$	Anion concentration
ε	0.025	$\frac{\mathrm{F}}{\mathrm{m}}$	Dielectric permittivity
l	200×10^{-6}	m	Length scale

3.2.1 Comparison of single mesh low-order FEM and *hp*-FEM

First of all, the low-order FEM and *hp*-FEM were compared. A single mesh H_ANISO with polynomial degrees $p = 1$ and $p = 2$ were compared to HP_ANISO mode. The coarse initial mesh as shown in Figure 3.2 (a) was used in the solutions. The results are shown in Figures 3.5 and 3.6.

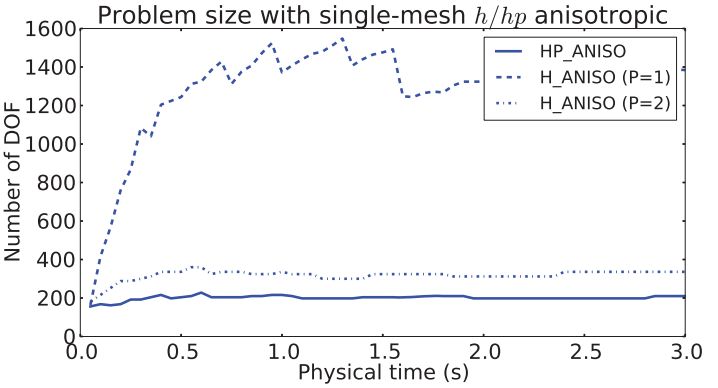

Figure 3.5: Number of degrees of freedom (DOF) as a function of physical time for single-mesh H_ANISO (in case of $p = 1$ and $p = 2$) and single-mesh HP_ANISO.

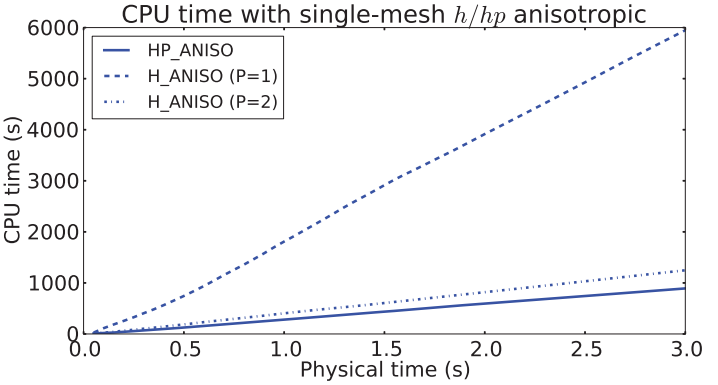

Figure 3.6: Cumulative CPU time as a function of physical time for single-mesh H_ANISO (in case of $p = 1$ and $p = 2$) and single mesh HP_ANISO.

It can be seen that *hp*-FEM results in a shorter computing time and smaller number of DOF than the low-order FEM. The same holds true for H_ISO and HP_ISO modes. In fact, in case of H_ISO the relative error did not

converge to the pre-set threshold value of 0.5% within acceptable range of degrees of freedom of $nDOF_{threshold} = 5000$. Therefore, the h-FEM solutions will be omitted from the further comparisons. Instead, only hp-FEM solutions on the coarse mesh and p-FEM solutions on the fine mesh will be discussed.

3.2.2 Comparison of single-mesh and multi-mesh *hp*-FEM

Running the simulation with different adaptivity modes and meshes showed that the multi-mesh hp-FEM configuration resulted in the smallest problems and similar error convergence compared to any single-mesh configuration. However, multi-mesh problems generally resulted in longer computing times. This is a known shortcoming of Hermes at this point and it is due to the fact that multi-mesh uses the union mesh where the numerical integration of high order is done on very small elements. The problem size and computing time are illustrated for HP_ANISO adaptivity mode in Figure 3.7 and Figure 3.8. The same holds true for HP_ISO mode. It must be also noted that the error converged to or below 0.5% for all p-FEM and anisotropic hp-FEM results.

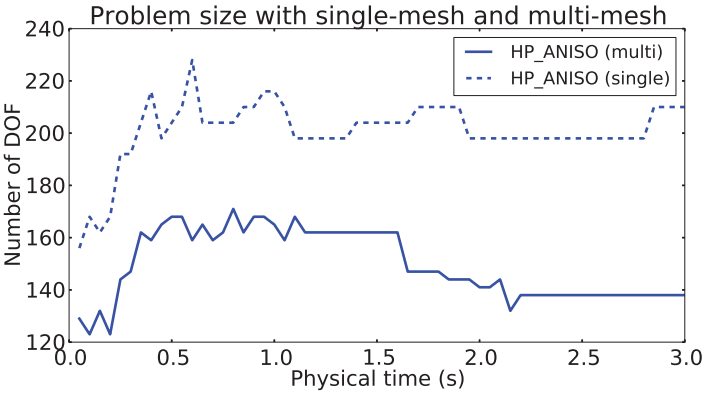

Figure 3.7: Number of DOF as a function of physical time for single-mesh and multi-mesh configurations with HP_ANISO adaptivity mode.

Figures 3.9 and 3.10 show higher-order meshes in the adaptive multi-mesh hp-FEM computation for c and φ at $t = 0.1$ s and $t = 3.0$ s, respectively. Different colors mean different polynomial degrees. A diagonal pattern inside an element tells that the element has different polynomial degrees in the horizontal and vertical directions.

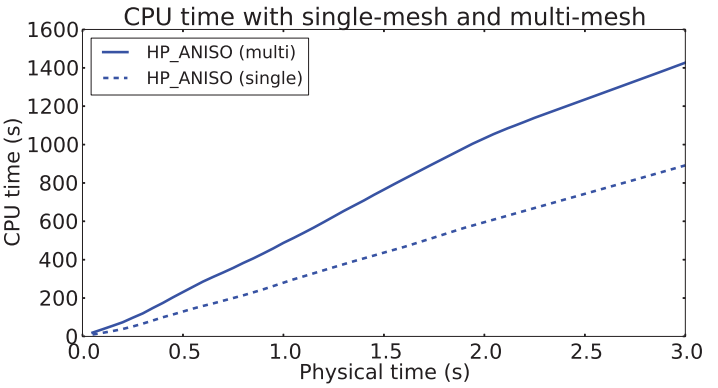

Figure 3.8: Cumulative CPU time as a function of physical time for single-mesh and multi-mesh configurations with HP_ANISO adaptivity mode.

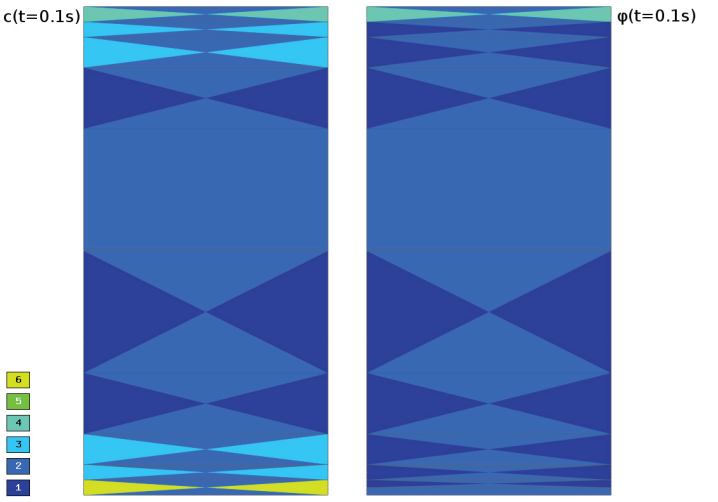

Figure 3.9: Higher-order FEM mesh for c and φ at $t = 0.1$ s.

The results are in good agreement with Figure 3.4 — in the vicinity of the boundaries $\partial\Omega_1$ and $\partial\Omega_3$, the concentration gradient is much greater than the voltage gradient. Therefore at $t = 0.1$ s, the multi-mesh hp-FEM adaptivity algorithm has increased the maximum polynomial degree for the c-space to 6 while the maximum polynomial degree for the φ-space is 4. The meshes are not that different in the beginning of the calculation. However, one can also see that the mesh refinement for c at $t = 3.0$ s is notably different compared to φ. For instance, the highest polynomial degree for c-space is 8 whereas for φ-space is 4. Since these results are representative

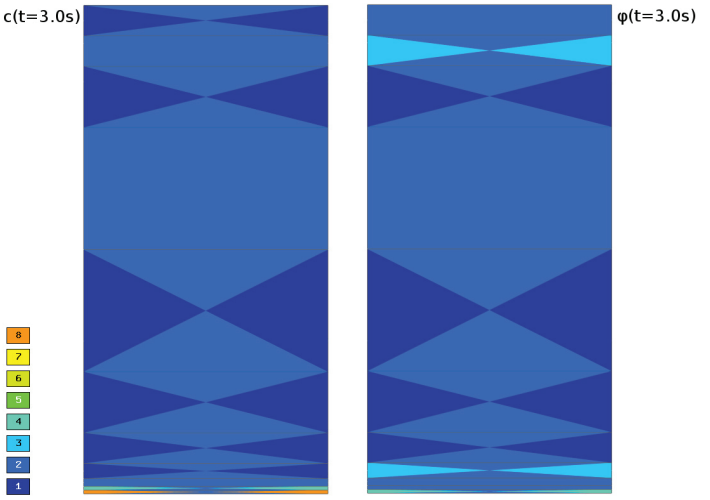

Figure 3.10: Higher-order FEM mesh for c and φ at $t = 3.0$ s.

for all adaptivity modes, only multi-mesh configurations are considered in the following.

3.2.3 Comparison of isotropic and anisotropic refinements

Next, the role of anisotropic mesh refinements is illustrated. Figures 3.11 and 3.12 show typical results for the HP_ISO, HP_ANISO_H, HP_ANISO adaptivity modes in terms of number of DOF and cumulative CPU time. Figure 3.13 shows corresponding error convergence. It can be seen that HP_ISO is notoriously inefficient as the error does not converge within the limited number of degrees of freedom of $nDOF_{threshold} = 5000$ and computing time is very large. Due to that fact, the calculation of HP_ISO was canceled before $t = 3.0$ s.

Figures 3.14 and 3.15 present a similar comparison for the P_ISO, P_-ANISO, and HP_ANISO_P modes. Recall that these computations use a different initial mesh that was a-priori refined in space.

As a conclusion, the reader can see that the anisotropic adaptivity modes always perform better than the isotropic ones. In particular, HP_ANISO results into the smallest problem size. In the p-adaptivity group, HP_-ANISO_P and P_ANISO lead to a small problem size consistently in each time step, whereas P_ISO yields large problems during the first time steps.

HP_ANISO also results in the fastest computing time among hp-adaptivity

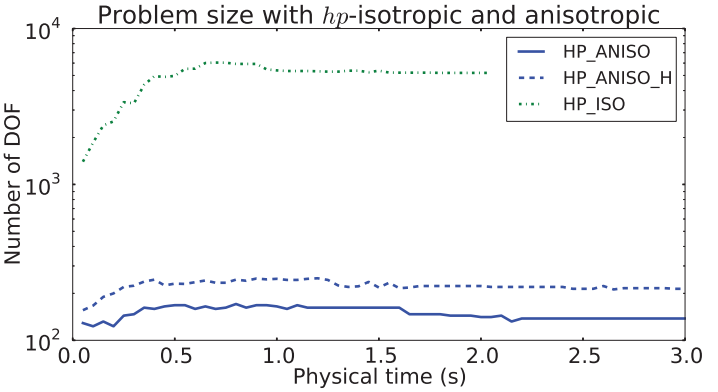

Figure 3.11: Number of DOF as a function of physical time for multi-mesh configurations with HP_ANISO, HP_ANISO_H, and HP_ISO adaptivity modes (log y scale).

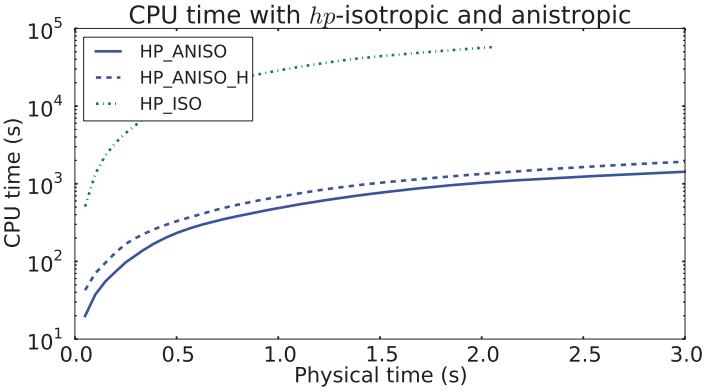

Figure 3.12: Cumulative CPU time as a function of physical time for multi-mesh configurations with HP_ANISO, HP_ANISO_H, and HP_ISO adaptivity modes (log y scale).

group whereas HP_ANISO_P results in the fastest overall computing time. This is due to the fact that HP_ANISO_P calculation is performed on the refined mesh. Regardless, the HP_ANISO adaptivity mode is the most suitable for the PNP problem due to the small size and relative fastness compared to the other adaptivity modes. A way to optimize the computing time of HP_ANISO will be considered next.

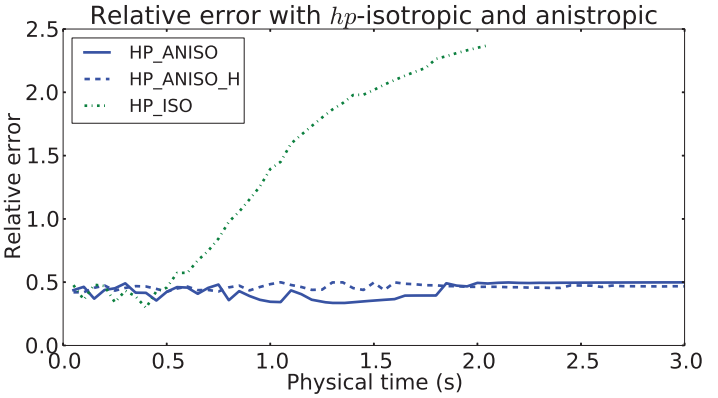

Figure 3.13: Relative solution error as a function of physical time for multi-mesh configurations with HP_ANISO, HP_ANISO_H, and HP_ISO adaptivity modes.

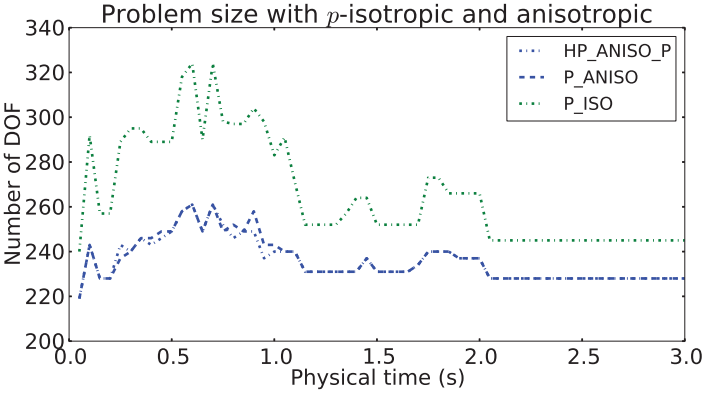

Figure 3.14: Number of DOF as a function of physical time for multi-mesh configurations with P_ISO, P_ANISO, and HP_ANISO_P adaptivity modes.

3.2.4 HP_ANISO adaptivity with physically more realistic boundary conditions

In real physics calculations, the applied voltage on boundary $\partial\Omega_1$ is not constant. This can be, for instance, due to the high resistance of the electrodes as explained in [67,80]. To see how the HP_ANISO adaptivity works for such situations, the voltage on the boundary was applied as follows:

$$\phi_{\Omega_1}(x) = 0.5\,[V]\,\frac{x\,[m]}{\mathrm{width}_{\Omega_1}\,[m]} + 0.5\,[V]\,, \tag{3.29}$$

where $\mathrm{width}_{\Omega_1}$ is the width of the boundary. The given boundary is effectively a linear increase of the voltage from $\phi_{\Omega_1}(x=0) = 0.5$ V to

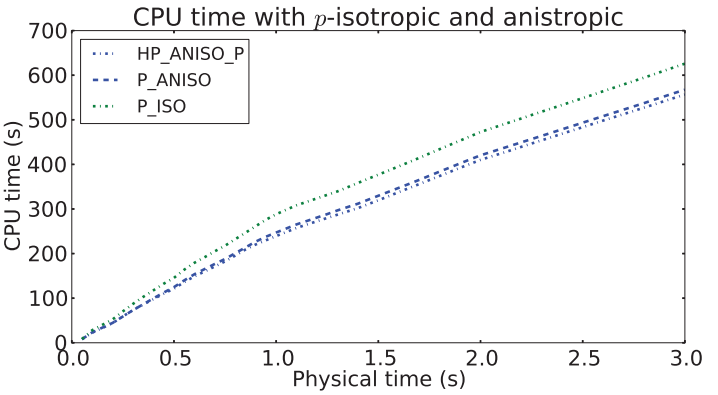

Figure 3.15: Cumulative CPU times as a function of physical time for multi-mesh configurations with P_ISO, P_ANISO, and HP_ANISO_P adaptivity modes.

$\phi_{\Omega_1}(x = \text{width}_{\Omega_1}) = 1.0$ V. Now the concentration gradient ∇c and the voltage gradient $\nabla\varphi$ are no longer effectively in 1D.

The calculated scaled values c and φ in Ω and corresponding meshes and polynomial degrees of the elements at $t = 0.1$ s are shown in Figure 3.16. Notice that the solution is different to the one in Figure 3.3. The HP_-ANISO adaptivity algorithm has particularly increased the polynomial degree and refined the mesh near Ω_1 where a sharp concentration peak exists (compare to Figure 3.9). At $t = 3.0$ s, the shape of the solutions c and φ are similar to the one in Figure 3.4 and therefore the polynomial space and mesh gets adapted accordingly. This example clearly illustrates how the solution of PNP with non-uniform boundary conditions is very dynamic in time and how the HP_ANISO time dependent adaptivity finds an optimal mesh and polynomial space to adapt to the dynamics of the problem.

3.2.5 Length scale analysis

The Debye length λ_D is the screening length in electrolyte solutions. Its numerical value shows the thickness of the charged layer in the vicinity of the boundaries $\partial\Omega_1$ and $\partial\Omega_2$. In all the previous simulations, the Debye screening length was determined by the constants in Table 3.1 and Eq. (3.6): $\lambda_D = 1.7$ μm. It is known that computation gets increasingly difficult when reducing the value of λ_D. It was an interest to see how small screening lengths can Hermes HP_ANISO automatic adaptivity handle. The parameter ε was varied as follows:

$$\varepsilon_n = \varepsilon \times 0.5^n,$$

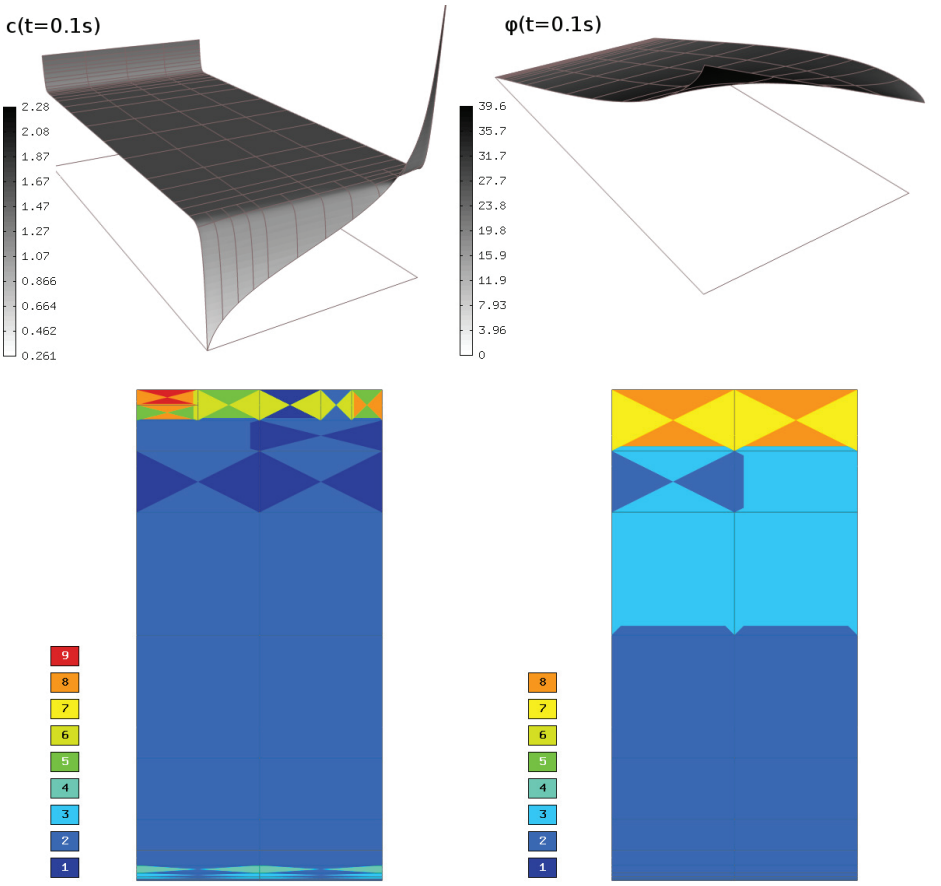

Figure 3.16: Solutions c and φ and corresponding polynomial degrees of the elements at $t = 0.1\ s$. HP_ANISO refinement mode was used. The height in the solution graphs indicates the value.

where ε is taken from Table 3.1. The simulations were run for each ε_n and corresponding λ_D value and maximum number of degrees of freedom and cumulative CPU time were recorded. The simulation time t for each λ_D was chosen to be τ — the characteristic time scale — and each simulation was divided equally into fifteen time steps. Time step adaptivity was not used. Figure 3.17 shows the maximum and average number of degrees of freedom during calculation as a function of the Debye length and Figure 3.18 shows cumulative CPU time as a function of the Debye length. The simulations up to 0.52 nm screening length were carried out on the initial coarse mesh. However, from $\lambda_D > 0.52$ nm, the finer initial mesh had to be used so the existence of the large gradients of the physical fields c and φ near the

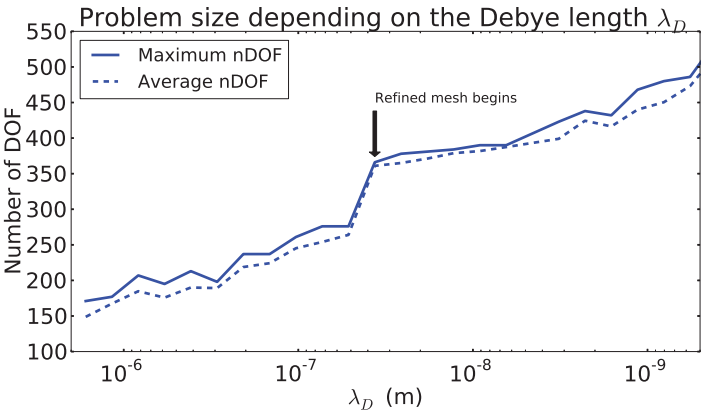

Figure 3.17: Problem size depending on the Debye length. Initially the coarse mesh (shown in Figure 3.2 (a)) was used. It was necessary to use the fine mesh (see Figure 3.2 (c)) for smaller λ_D values.

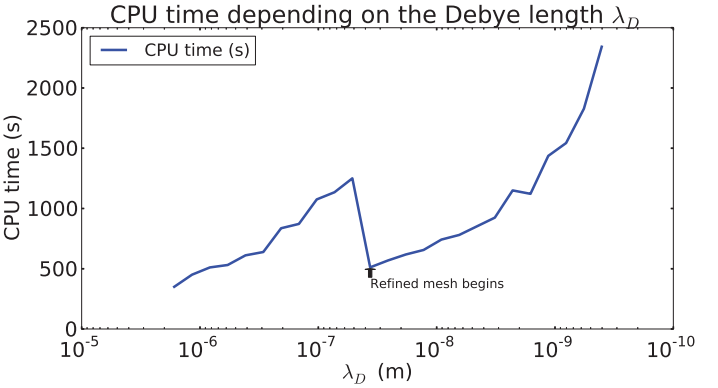

Figure 3.18: CPU time depending on the Debye length. Initially the coarse mesh (shown in Figure 3.2 (a)) was used. It was necessary to use the fine mesh (see Figure 3.2 (c)) for smaller λ_D values.

boundaries could be captured in the first place.

The fine mesh allowed simulations with the Debye length down to 0.40 nm. The calculated c and φ at $t = \tau$ for $\lambda_D = 0.40$ nm are shown in Figure 3.19. It appears that when using even finer initial mesh and higher initial polynomial degrees, even smaller Debye lengths could be used when necessary. The polynomial space of c had consistently higher maximum polynomial degree than that of φ, however, the difference was less noticeable for smaller Debye lengths.

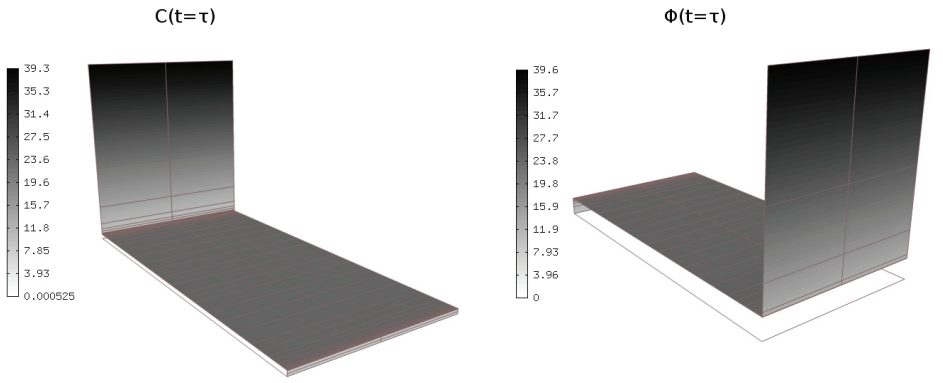

Figure 3.19: Calculated fields c and φ at $t = \tau = 0.81\ ms$ for $\lambda_D = 0.4\ nm$.

3.3 Chapter conclusions

It was shown that using the time dependent adaptivity, multi-mesh configuration, and anisotropic *hp* refinements, the PNP problem size remains very small throughout the solving process while maintaining a pre-set relative error of the solution. Hermes refinement mode HP_ANISO resulted in the smallest and fastest problem solution. Furthermore, using the multi-mesh configuration for the physical fields c and φ — scaled variables for C and ϕ, respectively — was justified. The adaptivity algorithm refined the meshes of φ and c and increased the polynomial degrees of the corresponding spaces differently. The mesh was significantly refined for c and also the maximum polynomial degree was varied in the range of $2 \ldots 9$ whereas for φ, the maximum polynomial degree remained lower. So it is efficient to use multi-mesh in terms of the number of degrees of freedom.

CHAPTER 4

hp-FEM MODEL OF IPMC DEFORMATION

In this chapter IPMC deformation is modeled via a multiphysics coupled problem consisting of the PNP equations and Navier's equations for displacement. These equations are used to calculate charge transport and resulting electromechanical transduction of the material. In order to find the best adaptive mode for this type of problems, numerous computations were performed using various adaptivity modes in single-mesh, multi-mesh with common mesh for displacement fields, and multi-mesh for all fields configurations. In the numerical experiments attention was paid to the relative error and problem size in terms of DOF at each time step. Based on the maximum relative error was fixed to 1.0%, a number of comparative calculation results is presented.

4.1 Deformation model

In order to calculate deformation of IPMC, the PNP system of equation is coupled with Navier's equation system for linear elastic material. For low frequency actuation, the time independent Navier's equation can be used to calculate deformation of IPMC as a function of time and local charge density in the material. Based on the strain-displacement relation

$$e_{ij} = \frac{1}{2}\left(u_{i,j} + u_{j,i}\right) \tag{4.1}$$

and equilibrium equation

$$\tau_{ij,j} + F_i = 0, \tag{4.2}$$

the constitutive equation of the linear elasticity is as follows:

$$\tau_{ij} = \lambda \delta_{ij} e_{kk} + 2\mu e_{ij}. \tag{4.3}$$

From there, the Navier's equation in the vector form can be expressed

$$(\lambda + \mu)\, u_{k,ki} + \mu u_{i,jj} + F_i = 0, \tag{4.4}$$

where u_i is a component of the displacement vector and F_i is a component of body force $(\frac{\mathrm{N}}{\mathrm{m}^3})$ [66]. Constants λ and μ are Lame's constants

$$\mu = \frac{E}{2\,(1+\nu)}, \quad \lambda = \frac{\nu E}{(1+\nu)\,(1-2\nu)} \tag{4.5}$$

where E is Young's modulus and ν Poisson's ratio. In 2D Cartesian coordinates Eq. (4.4) takes the form

$$(\lambda + \mu)\left(\frac{\partial^2 u_1}{\partial x^2} + \frac{\partial^2 u_2}{\partial y \partial x}\right) + \mu\left(\frac{\partial^2 u_1}{\partial x^2} + \frac{\partial^2 u_1}{\partial y^2}\right) + F_1 = 0, \tag{4.6}$$

$$(\lambda + \mu)\left(\frac{\partial^2 u_1}{\partial x \partial y} + \frac{\partial^2 u_2}{\partial y^2}\right) + \mu\left(\frac{\partial^2 u_2}{\partial x^2} + \frac{\partial^2 u_2}{\partial y^2}\right) + F_2 = 0. \tag{4.7}$$

In case of IPMC electromechanical transduction model, $F_2 = 0$ and F_1 can be expressed as a function of cation concentration $F_1 = A\,(C - C_0)$, where A is a constant [67]. In the following derivation, we consider a rectangular 2D domain $\Omega \subset \mathbb{R}^2$ with boundaries $\partial\Omega_{1\ldots4} \subset \partial\Omega$, shown in Figure 4.1. It is similar to the domain shown in Figure 3.1, except it is longer in the x-direction to present a cross-section of IPMC more realistically.

For the Navier's Eqs. (4.6) and (4.7), the following Dirichlet BCs are applied:

$$u_{1_{\partial\Omega_2}} = u_{2_{\partial\Omega_2}} = 0. \tag{4.8}$$

As no external forces are considered, zero Neumann BCs are applied on $\partial\Omega$:

$$\tau_{ij} n_j \,|_{\,\partial\Omega} = 0. \tag{4.9}$$

To make the results easily reproducible, in the following we present the derivation of weak forms of (4.6) and (4.7) as well as formulas for the Jacobian matrix and residual vector for the entire PNP-Navier's system of equations that are used in the deformation computations.

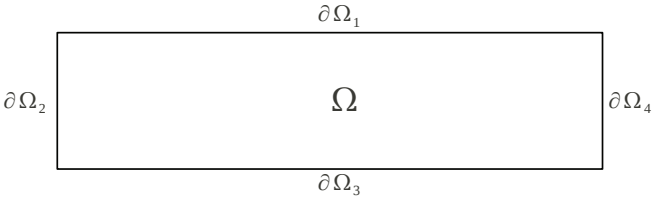

Figure 4.1: Calculation domain $\Omega \subset \mathbb{R}^2$ with boundaries $\partial\Omega_{1\ldots4} \subset \partial\Omega$.

4.1.1 Weak form of the equations

As in case of the PNP system, a dimensionless formulation of Navier's Eqs. (4.6) and (4.7) is derived by denoting the components of displacement field:

$$U_1 = \frac{u_1}{l}, \quad U_2 = \frac{u_2}{l}. \tag{4.10}$$

It could be observed from Eqs. (3.5) and (4.10) that in the dimensionless formulation, variables with the unit of meter are in the upper case, whereas other variables are in the lower case. After inserting variables (4.10) as well as variable c into (4.6), the Navier's equations become:

$$(\lambda+\mu)\left(\frac{\partial^2 U_1}{\partial X^2}+\frac{\partial^2 U_2}{\partial X \partial Y}\right)+\mu\left(\frac{\partial^2 U_1}{\partial X^2}+\frac{\partial^2 U_1}{\partial Y^2}\right) = AlC_0\,(1-c)\,, \tag{4.11}$$

$$(\lambda+\mu)\left(\frac{\partial^2 U_1}{\partial X \partial Y}+\frac{\partial^2 U_2}{\partial Y^2}\right)+\mu\left(\frac{\partial^2 U_2}{\partial X^2}+\frac{\partial^2 U_2}{\partial Y^2}\right) = 0. \tag{4.12}$$

As in the case of the weak form of the PNP system, Sobolev space is used for the test functions. First, we multiply Eq. (4.11) with a test function $v^{U_1} \in V$ and integrate over domain Ω. By applying the zero external boundary conditions, the resulting final weak form of (4.11) is expressed:

$$\begin{aligned}(2\mu+\lambda)\int_\Omega \frac{\partial U_1}{\partial X}\frac{\partial v^{U_1}}{\partial X}d\mathbf{x}+\lambda\int_\Omega \frac{\partial U_2}{\partial Y}\frac{\partial v^{U_1}}{\partial X}d\mathbf{x}\\ +\mu\int_\Omega \frac{\partial U_1}{\partial Y}\frac{\partial v^{U_1}}{\partial Y}+\frac{\partial U_2}{\partial X}\frac{\partial v^{U_1}}{\partial Y}d\mathbf{x}\\ +lAC_0\int_\Omega (1-c)\,v^{U_1}d\mathbf{x}=0.\end{aligned} \tag{4.13}$$

Dimensionless formulation of the equation can be obtained by first writing constants μ and λ explicitly in terms of ν and E and then multiplying the

equation by $(1+\nu)/E$:

$$\left(1+\frac{\nu}{1-2\nu}\right)\int_\Omega \frac{\partial U_1}{\partial X}\frac{\partial v^{U_1}}{\partial X}d\mathbf{x}+\frac{\nu}{1-2\nu}\int_\Omega \frac{\partial U_2}{\partial Y}\frac{\partial v^{U_1}}{\partial X}d\mathbf{x} +\frac{1}{2}\int_\Omega \frac{\partial U_1}{\partial Y}\frac{\partial v^{U_1}}{\partial Y}+\frac{\partial U_2}{\partial X}\frac{\partial v^{U_1}}{\partial Y}d\mathbf{x} +\frac{1+\nu}{E}C_0 lA\int_\Omega (1-c)\,v^{U_1}d\mathbf{x}=0. \tag{4.14}$$

Now the LHS consist only dimensionless constants and variables and the displacements are governed solely by the RHS term that consists of material properties and is also a function of cation concentration c. Similarly, the weak form of Eq. (4.12) is:

$$\left(1+\frac{\nu}{1-2\nu}\right)\int_\Omega \frac{\partial U_2}{\partial Y}\frac{\partial v^{U_2}}{\partial Y}d\mathbf{x}+\frac{\nu}{1-2\nu}\int_\Omega \frac{\partial U_1}{\partial X}\frac{\partial v^{U_2}}{\partial Y}d\mathbf{x} +\frac{1}{2}\int_\Omega \frac{\partial U_2}{\partial X}\frac{\partial v^{U_2}}{\partial X}+\frac{\partial U_1}{\partial Y}\frac{\partial v^{U_2}}{\partial X}d\mathbf{x}=0. \tag{4.15}$$

4.1.2 Jacobian matrix components and residual vector

To employ the Newton's method on the entire nonlinear system (3.17), (3.19), (4.14), and (4.15), formulas for the Jacobian matrix and residual vector need to be derived. As for the PNP system in Chapter 3, time discretization will be performed using the second-order Crank-Nicolson method.

The coefficient vector $\mathcal{Y}^{n+1}$ (see (3.20) and (3.21)) length is $N^c+N^\varphi+N^{U_1}+N^{U_2}$ comprising the unknown solution coefficients y_k^c, y_k^φ, $y_k^{U_1}$, and $y_k^{U_2}$ (in this order). Also, $c^n=c(\mathcal{Y}^n)$, $\varphi^n=\varphi(\mathcal{Y}^n)$, $U_1^n=U_1(\mathcal{Y}^n)$, and $U_2^n=U_2(\mathcal{Y}^n)$ will be used for the previous time step solutions. Based on that, the first and the second component of the residual vector are unchanged and described with Eqs. (3.22) and (3.23). The third and fourth component of the residual vector can be respectively written:

$$\mathcal{F}_i^{U_1}(\mathcal{Y})=\left(1+\frac{\nu}{1-2\nu}\right)\int_\Omega \frac{\partial U_1(\mathcal{Y})}{\partial X}\frac{\partial v^{U_1}}{\partial X}d\mathbf{x} +\frac{\nu}{1-2\nu}\int_\Omega \frac{\partial U_2(\mathcal{Y})}{\partial Y}\frac{\partial v^{U_1}}{\partial X}d\mathbf{x} +\frac{1}{2}\int_\Omega \frac{\partial U_1(\mathcal{Y})}{\partial Y}\frac{\partial v^{U_1}}{\partial Y}+\frac{\partial U_2(\mathcal{Y})}{\partial X}\frac{\partial v^{U_1}}{\partial Y}d\mathbf{x} +\frac{1+\nu}{E}C_0 lA\int_\Omega (1-c(\mathcal{Y}))\,v^{U_1}d\mathbf{x}, \tag{4.16}$$

and

$$\mathcal{F}_i^{U_2}(\mathcal{Y}) = \left(1+\frac{\nu}{1-2\nu}\right)\int_\Omega \frac{\partial U_2(\mathcal{Y})}{\partial Y}\frac{\partial v^{U_2}}{\partial Y}d\mathbf{x} + \frac{\nu}{1-2\nu}\int_\Omega \frac{\partial U_1(\mathcal{Y})}{\partial X}\frac{\partial v^{U_2}}{\partial Y}d\mathbf{x} + \frac{1}{2}\int_\Omega \frac{\partial U_2(\mathcal{Y})}{\partial X}\frac{\partial v^{U_2}}{\partial X} + \frac{\partial U_1(\mathcal{Y})}{\partial Y}\frac{\partial v^{U_2}}{\partial X}d\mathbf{x}. \quad (4.17)$$

The nonlinear discrete problem that needs to be solved at the end of each time step has the form $\mathcal{F}(\mathcal{Y}) = 0$. The Jacobian matrix $\mathcal{J}(\mathcal{Y}) = D\mathcal{F}/D\mathcal{Y}$ has now a 4×4 block structure, and its entries are obtained by calculating the partial derivatives of $\mathcal{F}$ with respect to the components of the coefficient vector $\mathcal{Y}$. New non-zero components of the matrix besides (3.25)–(3.28) are:

$$\frac{\partial \mathcal{F}_i^{U_1}}{\partial y_j^c}(\mathcal{Y}) = -\frac{1+\nu}{E}C_0 lA\int_\Omega v_j^c v_i^{U_1}d\mathbf{x}, \quad (4.18)$$

$$\frac{\partial \mathcal{F}_i^{U_1}}{\partial y_j^{U_1}}(Y) = \left(1+\frac{\nu}{1-2\nu}\right)\int_\Omega \frac{\partial v_j^{U_1}}{\partial X}\frac{\partial v_i^{U_1}}{\partial X}d\mathbf{x} + \frac{1}{2}\int_\Omega \frac{\partial v_j^{U_1}}{\partial Y}\frac{\partial v_i^{U_1}}{\partial Y}d\mathbf{x}, \quad (4.19)$$

$$\frac{\partial \mathcal{F}_i^{U_1}}{\partial y_j^{U_2}}(\mathcal{Y}) = \frac{\nu}{1-2\nu}\int_\Omega \frac{\partial v_j^{U_2}}{\partial Y}\frac{\partial v_i^{U_1}}{\partial X}d\mathbf{x} + \frac{1}{2}\int_\Omega \frac{\partial v_j^{U_2}}{\partial X}\frac{\partial v_i^{U_1}}{\partial Y}d\mathbf{x}, \quad (4.20)$$

$$\frac{\partial \mathcal{F}_i^{U_2}}{\partial y_j^{U_1}}(\mathcal{Y}) = \frac{\nu}{1-2\nu}\int_\Omega \frac{\partial v_j^{U_1}}{\partial X}\frac{\partial v_i^{U_2}}{\partial Y}d\mathbf{x} + \frac{1}{2}\int_\Omega \frac{\partial v_j^{U_1}}{\partial Y}\frac{\partial v_i^{U_2}}{\partial X}d\mathbf{x}, \quad (4.21)$$

$$\frac{\partial \mathcal{F}_i^{U_2}}{\partial y_j^{U_2}}(\mathcal{Y}) = \left(1+\frac{\nu}{1-2\nu}\right)\int_\Omega \frac{\partial v_j^{U_2}}{\partial Y}\frac{\partial v_i^{U_2}}{\partial Y}d\mathbf{x} + \frac{1}{2}\int_\Omega \frac{\partial v_j^{U_2}}{\partial X}\frac{\partial v_i^{U_2}}{\partial X}d\mathbf{x}. \quad (4.22)$$

4.2 Numeric results

The PNP-Navier's problem was implemented in Hermes and a large number of calculations were carried out in order to find the best adaptivity mode

for the problem. Based on the study in Chapter 3, isotropic adaptivities were not consider as these performed the worst. The study and results are structured similar to the PNP system study presented in Chapter 3.

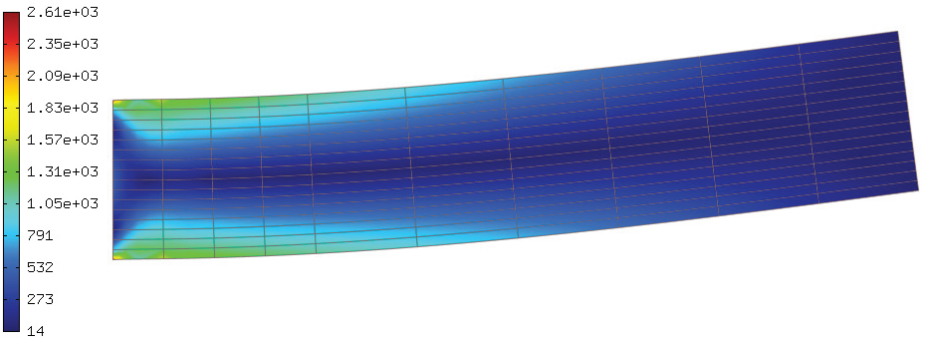

Figure 4.2: Example deformation of IPMC calculated with Hermes *hp*-FEM software package. The color indicates local von Mises stress.

The computations were performed using various adaptivity modes in (a) single-mesh, (b) multi-mesh with common mesh for displacement fields, and (c) multi-mesh for all fields configurations. The maximum relative error was fixed to 1.0% in this study. An example deformation of IPMC calculated with Hermes is shown in Figure 4.2.

4.2.1 Advantages of multi-mesh *hp*-FEM

Simulations with different adaptivity modes and meshes showed that the multi-mesh *hp*-FEM configuration results in the smallest problems compared to any single-mesh configuration. At the same time, the computing time and error convergence were similar for all cases. For instance, single vs. multi-meshes comparison for the HP_ANISO adaptivity mode are shown in Figures 4.3 and 4.4.

Displacement fields U_1 and U_2 are similar in terms of gradient and very different from c and φ. Therefore, one of the multi-mesh configuration was based on three different meshes – a mesh for c, a mesh for φ, and a common mesh for U_1 and U_2. Interestingly, the "true" multi-mesh (separate mesh for each field) turned out to be the most efficient configuration compared to the others – calculation on the optimized meshes balances the CPU cost of calculate the meshes (Figure 4.4) while keeping the problem size the

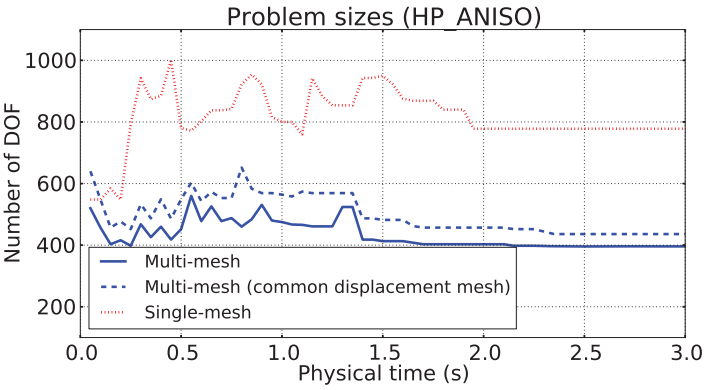

Figure 4.3: Number of DOFs as a function of physical time for single-mesh and multi-mesh configurations with HP_ANISO adaptivity mode.

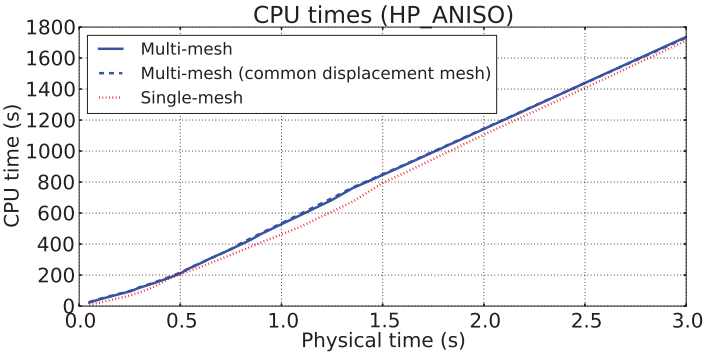

Figure 4.4: Cumulative CPU time as a function of physical time for single-mesh and multi-mesh configurations with HP_ANISO adaptivity mode.

smallest (Figure 4.3). Thus, in all of the following simulations, only the multi-mesh configuration is used.

4.2.2 Anisotropic refinements

The calculations were carried out with three different anisotropic adaptivity modes – HP_ANISO, HP_ANISO_H, and HP_ANISO_P. It was already shown that the rest of the adaptivity types (isotropic, P_ANISO, H_ANISO) do not perform well for this type of multiphysics problems [81]. For instance, in case of p-adaptivities it is necessary to know the problem and gradients rather well to start with a suitable initial mesh or the error might never converge below a pre-set limit. At the same time, HP_ANISO,

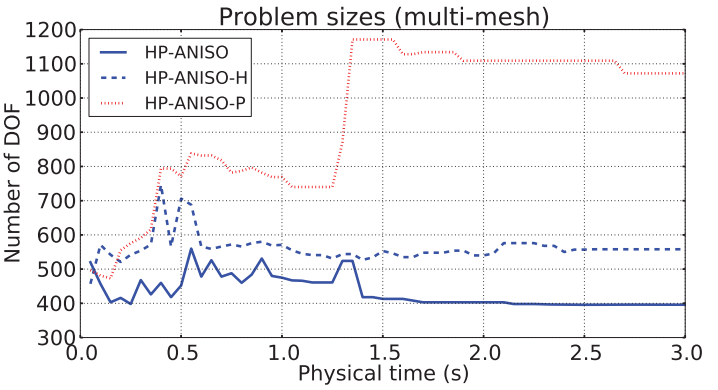

Figure 4.5: Problem size with different adaptivity modes in the multi-mesh configuration.

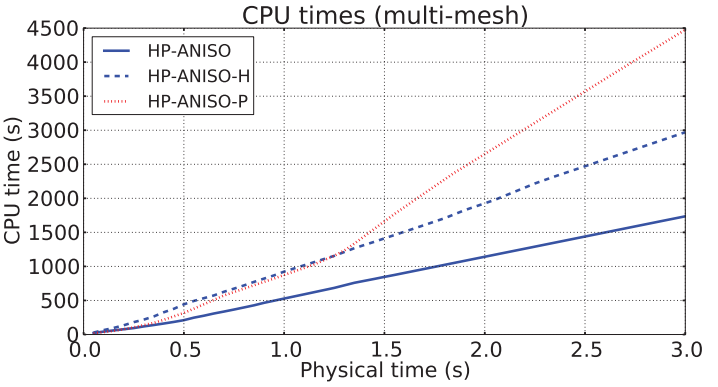

Figure 4.6: CPU time with different adaptivity modes in the multi-mesh configuration.

HP_ANISO_H, and HP_ANISO_P all perform relatively well. Thus, in this study an attempt was made to determine which one of them is the most suitable for such a coupled problem as is the time dependent IPMC actuation.

It can be seen in Figures 4.5 and 4.6 that both the problem size and CPU time are consistently smallest for HP_ANISO adaptivity. Interestingly, in the case of HP_ANISO_P, both CPU time and number of DOF start rapidly increasing at the point where the other modes stabilize. It can be attributed to the isotropic h-refinements for the steep boundary gradients. Namely, Figure 4.7 shows the number of adaptive steps (main plot) it takes to reach to the desired error level (Figure 4.7 subplot). Although the number of steps

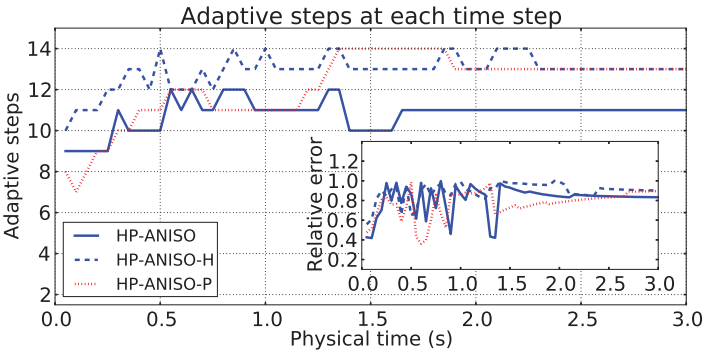

Figure 4.7: Number of adaptive steps at each time (main plot) and final relative error between a coarse and fine mesh solutions (sub-plot).

for HP_ANISO_P stabilizes close to HP_ANISO_H (13 adaptivity steps per time step), the latter is more efficient – apparently, isotropic h-adaptivity is a rather expensive way to reduce the error of a solution.

To illustrate the effectiveness of HP_ANISO, a snapshot of the meshes and polynomial degrees were recorded for each of the fields. Figure 4.8 shows the magnitudes and meshes for c, φ, U_1 and U_2 at $t = 0.1$ s. The mesh is significantly adapted near the $\partial\Omega_1$ and $\partial\Omega_3$ boundaries for c and φ – this can be explained by the steep gradients of these fields (as shown in Figure 1.4). On the other hand, the displacement field mesh is rather coarse. In case of U_1, some of the elements are split vertically whereas in most of the elements, no vertical splits occur. Figure 4.9 shows local polynomial degrees for the fields at the same time. Again, due to the steep gradient of c near $\partial\Omega_3$, the polynomial degree near that boundary is 8. For other fields, the maximum polynomial degrees are mostly equal or less than 4. Overall, the HP_ANISO adaptivity mode appears to be the most suitable for the such multi-field multiphysics problem due to the resulting small problem size and relative fastness compared to the other anisotropic adaptivities.

4.2.3 Calculations with more advanced BCs

In the previous section, HP_ANISO, HP_ANISO_H, and HP_ANISO_P adaptivity modes were compared for constant voltage BCs. In more practical calculations, the applied voltages on the boundaries $\partial\Omega_1$ and $\partial\Omega_3$ have to be considered as gradients rather than constants. This can be, for instance, due to electrical resistance of the electrodes or underlying elec-

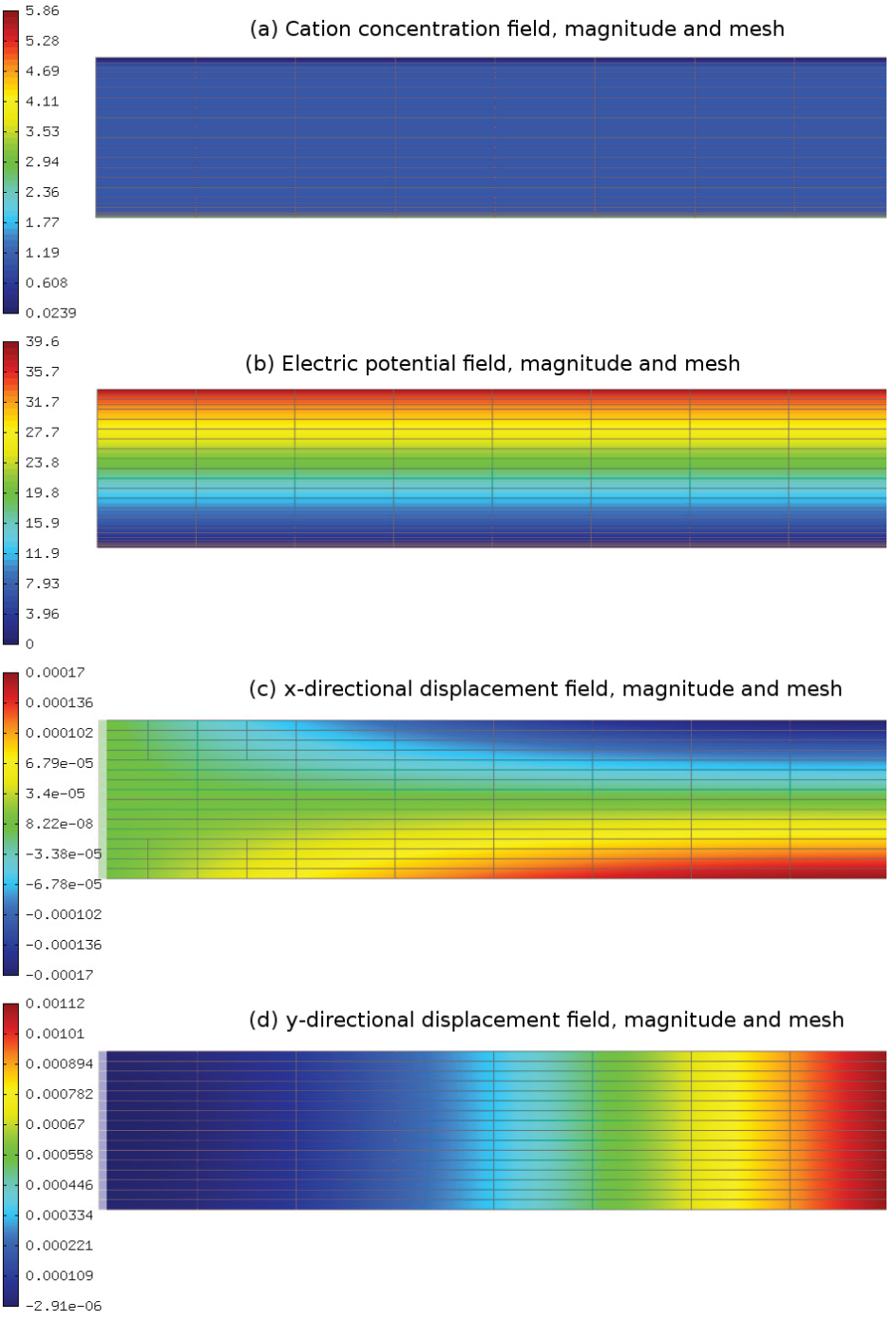

Figure 4.8: c, φ, U_1, and U_2 field meshes and magnitudes at $t = 0.1$ s in (a), (b), (c), and (d), respectively. Notice that the meshes are optimized for the particular fields.

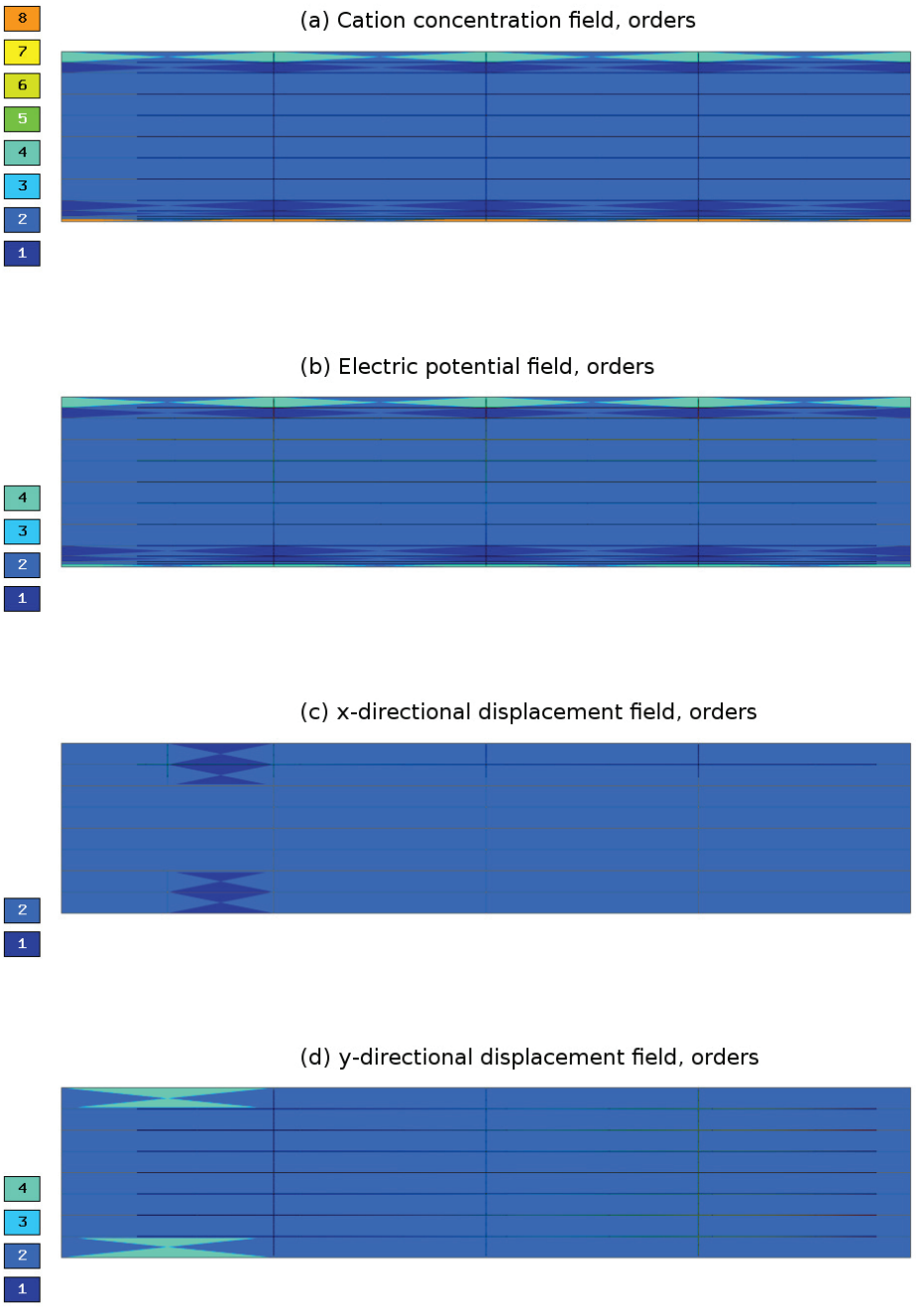

Figure 4.9: c, φ, U_1, and U_2 field polynomial degrees at $t = 0.1$ s in (a), (b), (c), and (d), respectively. Higher order elements are used in case of c and φ due to steep boundary gradients.

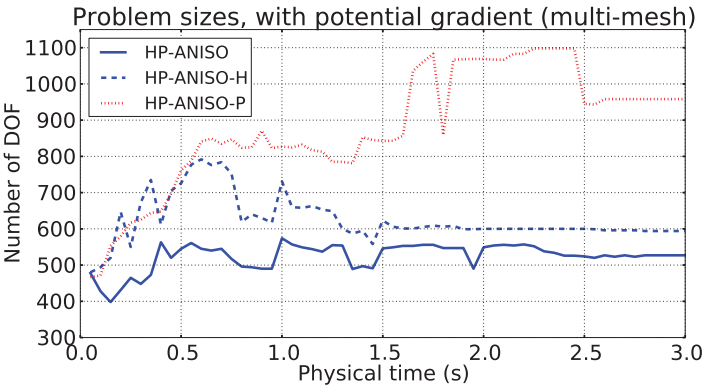

Figure 4.10: Problem size with different adaptivity modes in the multi-mesh configuration and applied potential gradient BCs.

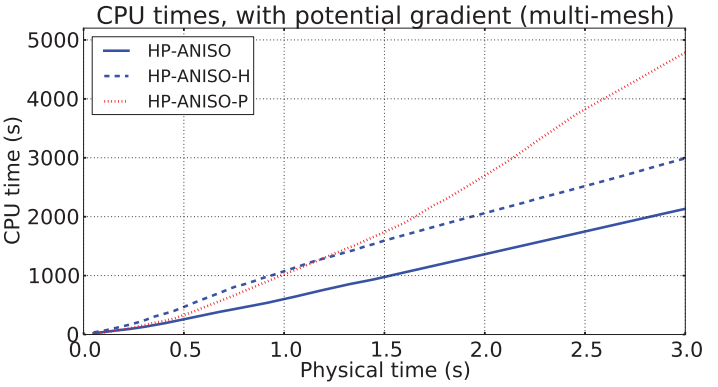

Figure 4.11: CPU time with different adaptivity modes in the multi-mesh configuration and applied potential gradient BCs.

trochemical currents as explained in [67]. In regular FEM calculations, a rather fine mesh has to be used as the boundary gradients can result in solution instability – the concentration gradient can peak in the corner of Ω (see Figure 4.1). To see how the anisotropic adaptivity modes perform, the potentials on these boundaries were applied as linear gradients. On $\partial\Omega_1$, the potential had linear drop of 25% from $x = 0$ toward the tip. Thus, for 1 V applied voltage, the tip voltage was 0.75 V. The same gradient was applied on $\partial\Omega_3$, i.e. from 0 V to 0.25 V at the tip. With the gradient BCs the concentration gradient ∇c and the voltage gradient $\nabla\varphi$ are no longer effectively in 1D. The goal of running simulations with multiple adaptivity types was to explore if additional x-directional gradients of c and φ would result in different adaptivity performances. It must be noted that in more

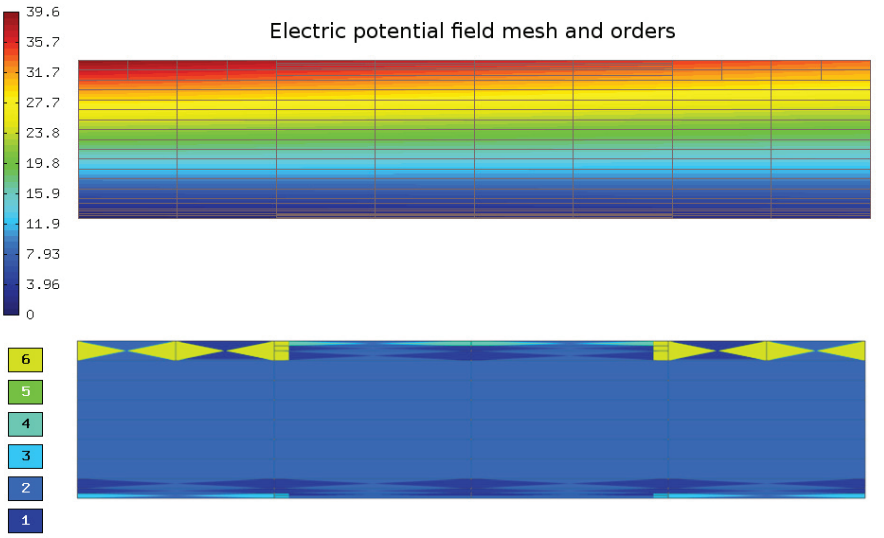

Figure 4.12: Calculated scaled φ field magnitude, mesh, and polynomial degrees with applied potential gradients along $\partial\Omega_1$ and $\partial\Omega_3$ at $t = 0.1$ s.

advanced calculations, the gradient is also dynamic, however, this would require considering the electrode domains and is not in the scope of this work.

Figures 4.10 and 4.11 show problem sizes and CPU times for different adaptivity modes with potential gradient BCs. It could be reasoned that HP_-ANISO_P can be a suitable as the x-directional gradient can require also vertical mesh refinements. However, as in the previous case, the HP_ANISO results in the smallest CPU time and problem size.

To illustrate, calculated φ in Ω and corresponding meshes and polynomial degrees of the elements at $t = 0.1$ s are shown in Figure 4.12. Notice that the solution and polynomial degrees are notably different to the ones in Figures 4.8 (b) and 4.9 (b). The HP_ANISO adaptivity algorithm has particularly increased the polynomial degree and refined the mesh near Ω_1 where a sharp concentration peaks occur due to the x-directional applied potential gradient. Also, the mesh is more refined. The effect is similar in case of c; however, it is easier to observe φ as the boundary is wider for the latter. This example clearly illustrates how the solution of the equations with non-uniform electric potential boundary conditions is dynamic and how the HP_ANISO time dependent adaptivity calculates an optimal mesh and polynomial space to adapt to the dynamics of the problem.

4.3 Chapter conclusions

IPMC electromechanical transduction was modeled by solving the system of PNP-Navier's equations using *hp*-finite element method with adaptive multi-mesh configuration. The meshes were significantly refined for c and φ and also the maximum polynomial degree was varied in the range of $2 \dots 8$ whereas for the displacement fields U_1 and U_2, the mesh variations were smaller; however, the polynomial degrees of the elements were increased where necessary. By using *hp*-FEM with adaptive multi-mesh configuration the problem size can be possibly reduced significantly while still maintaining a prescribed precision of the solution.

CHAPTER 5

SCALABILITY AND OPTIMIZATIONS

In this chapter it is shown how *hp*-FEM helps to keep the IPMC deformation model geometrically scalable while solutions maintain pre-set relative error. Additionally, it is shown how employing a PID controller based time step adaptivity helps to reduce the calculation time. Data presented in Chapters 3 and 4 shows that HP_ANISO adaptivity results in the best performance compared to other anisotropic adaptivity types. Therefore, HP_ANISO adaptivity was chosen as the adaptivity type for all the calculations in this chapter.

5.1 Geometric scalability

Geometric scalability study is presented for the PNP-Navier's system of equations (Chapter 4). The derived model was applied on domains with different aspect ratios to study how *hp*-FEM performs in terms of numbers of degrees of freedom and CPU time.

Although the typical length of an IPMC is in the range of 1 cm and above, the calculations were carried out for 1 mm long IPMC. It turns out that increasing the length of the calculation domain will not result in significant penalty both in problem size and CPU time. For the most part, the gradients in the longitudinal direction are small – even in case a potential drop along the boundaries $\partial\Omega_1$ and $\partial\Omega_3$ is considered (see Figure 4.1).

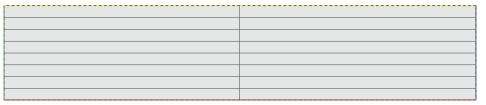

Figure 5.1: 0.2 mm thick IPMC initial mesh.

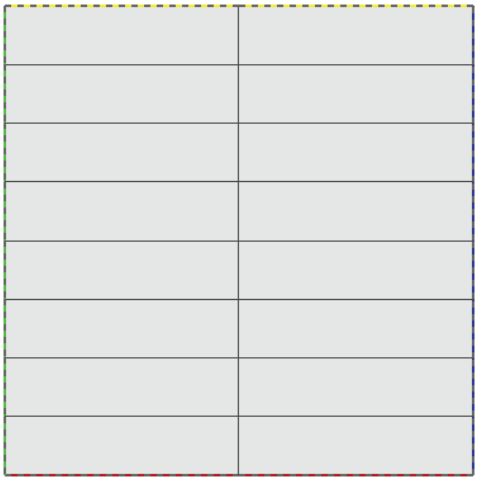

Figure 5.2: 1.0 mm thick IPMC initial mesh.

On the other hand, very steep gradients form in the thickness direction of IPMC. To study how *hp*-FEM performs for different IPMC dimensions, calculations were carried out for 0.2 mm, 0.5 mm, and 1.0 mm thick IPMCs. The initial mesh was same for each thickness (see Figure 5.1 for 0.2 mm long domain and Figure 5.2 for 1.0 mm long domain).

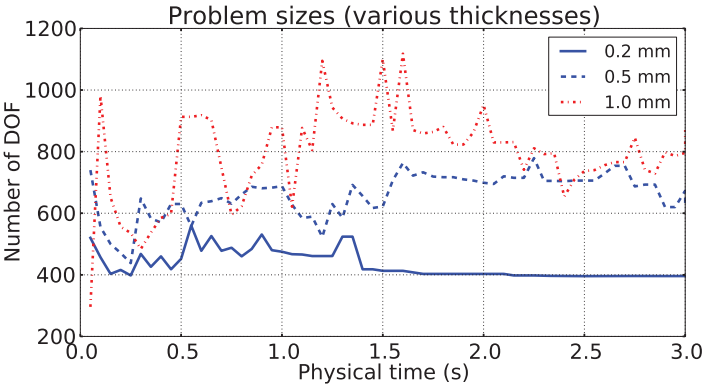

Figure 5.3: Problem size each time step for 0.2 mm, 0.5 mm, and 1.0 mm thick calculation domains.

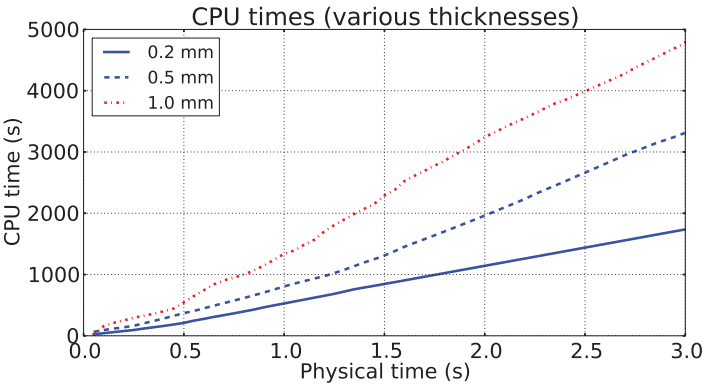

Figure 5.4: CPU times at each time step for 0.2 mm, 0.5 mm, and 1.0 mm thick calculation domains.

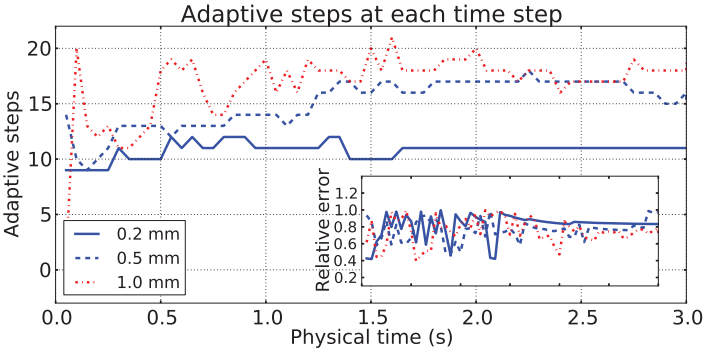

Figure 5.5: Number of adaptivity steps time with final relative error (sub-plot) at each time step for 0.2 mm, 0.5 mm, and 1.0 mm thick calculation domains.

Figure 5.3 shows that the problem size depends on the domain thickness only slightly. It can be expected as the major field gradients ($\nabla_d c$ and $\nabla_d \varphi$) still form near the electrode boundaries. However, the CPU time does increase noticeably with the thickness – see Figure 5.4. To investigate the reasons for it, the number of adaptivity steps it takes to reach to the desired error level (Figure 5.5 subplot) was recored at each time step (Figure 5.5 main plot). Interestingly, it takes almost twice as many steps to reach to the pre-set 1.0% error for 1.0 mm IPMC compared to that of 0.2 mm IPMC.

Automatically refined meshes, field magnitudes, and polynomial spaces were captured for 0.2 mm and 1.0 mm thick IPMCs at $t = 0.1\,\mathrm{s}$ to understand why the thicker IPMCs require that many extra adaptivity steps

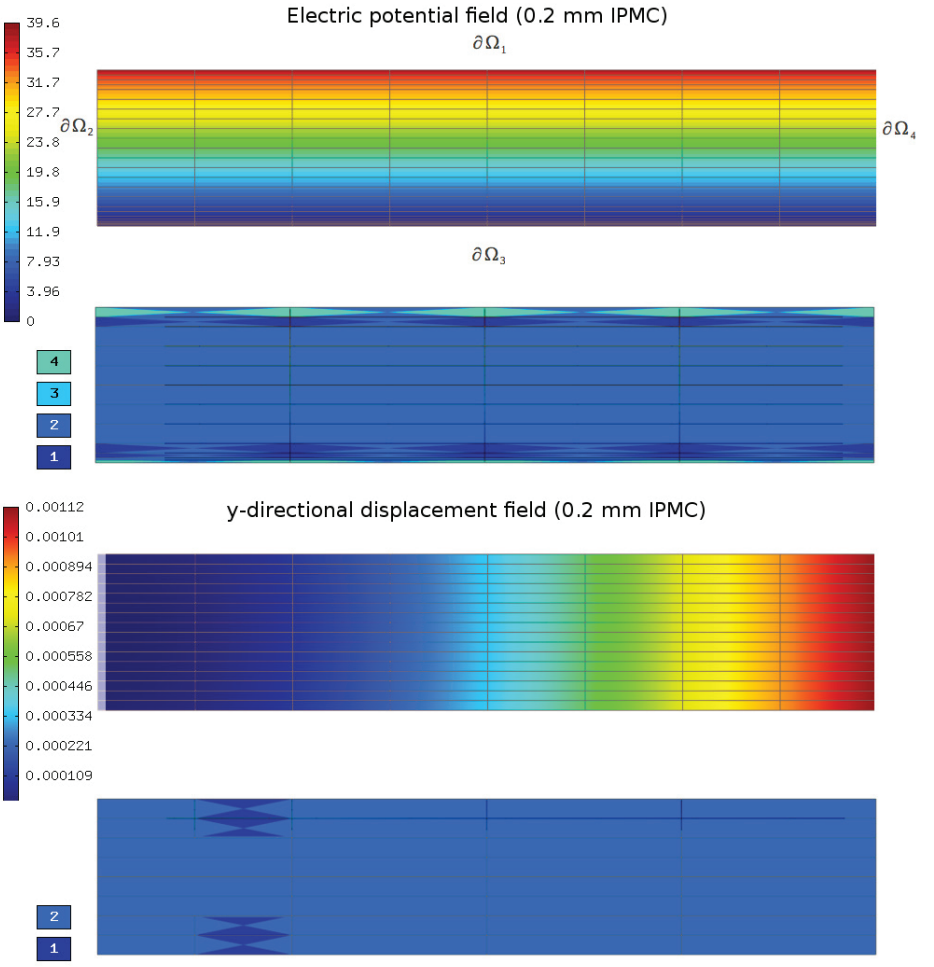

Figure 5.6: 0.2 mm thick IPMC calculation snapshot at $t = 0.1\,\mathrm{s}$. Mesh and magnitudes of φ and U_2 (left); polynomial degrees of φ and U_2 (right).

(Figures 5.6 and 5.7). It can be seen that the displacement field calculation for 1.0 mm IPMC requires considerably finer mesh and higher polynomial degrees near $\partial\Omega_2$ – the effect of the fixed boundary is far more significant for a thick IPMC than for the 0.2 mm one with the same length. Refinements of the y-directional displacement field occur near the corners and inside the domain for the 1.0 mm IPMC and some elements have the polynomial degree of 7. At the same time, potential field φ has the maximum polynomial degree of 4 and the meshes have been refined only near the boundaries $\partial\Omega_1$

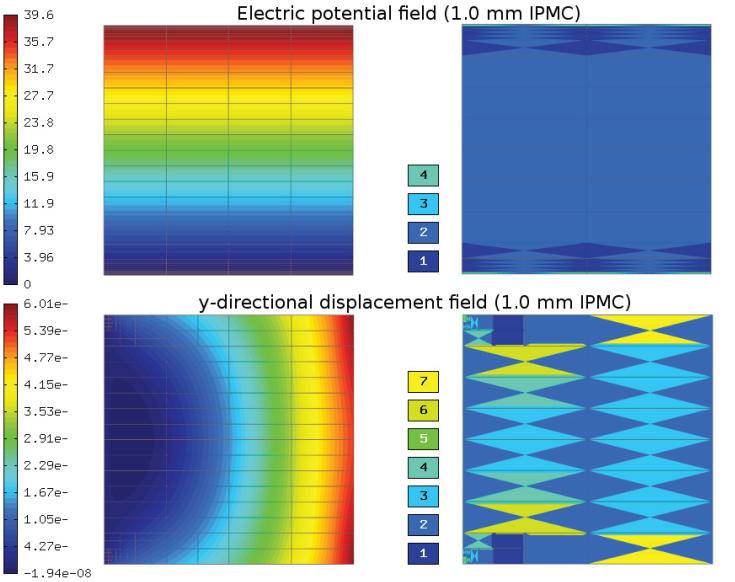

Figure 5.7: 1.0 mm thick IPMC calculation snapshot at $t = 0.1\,\mathrm{s}$. Mesh and magnitudes of φ and U_2 (left); polynomial degrees of φ and U_2 (right).

and $\partial\Omega_3$ for both thicknesses, but the refinements are more significant near $\partial\Omega_1$ for 1.0 mm IPMC.

This example demonstrates how *hp*-FEM adaptive algorithm can be beneficial in determining an optimal mesh and polynomial space for such dynamic multi-physics problem. Using a static mesh that is refined near the boundaries can work for some cases, but comparison of Figures 5.6 and 5.7 show how it might not be always sufficient to get precise calculation results while maintaining a small problem size.

5.2 PID time step control

Although *hp*-FEM adaptive algorithms help to maintain a relatively small problem size in terms of number of DOF during a time dependent calculation process, the CPU time can be potentially very high due to a large number of adaptivity steps. This is especially noticeable in case of the dynamic problems where the base mesh (such as shown in Figure 3.2) is loaded in the beginning of each time step. To optimize the calculation time of HP_ANISO, an adaptive time step control is employed. The classical PID controller is used [78]. Since c, φ, U_1, and U_2 change differently in

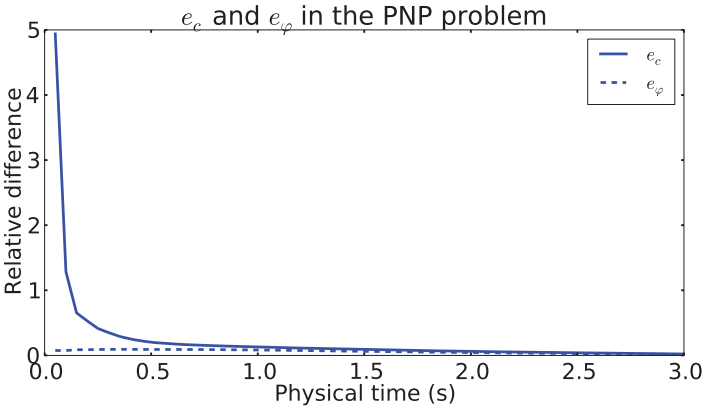

Figure 5.8: Relative difference e_c^n and e_φ^n.

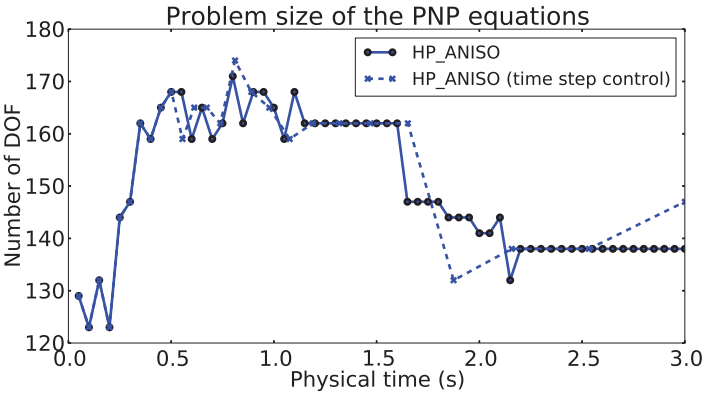

Figure 5.9: Number of DOF as a function of physical time for HP_ANISO with and without time step adaptivity. The markers on the graphs indicate the time steps.

time, the relative changes between the solutions at different time steps are monitored:

$$e_c^n = \frac{\left\|c^n - c^{n-1}\right\|}{\|c^n\|}, \tag{5.1}$$

$$e_\varphi^n = \frac{\left\|\varphi^n - \varphi^{n-1}\right\|}{\|\varphi^n\|}, \tag{5.2}$$

$$e_{U_1}^n = \frac{\left\|U_1^n - U_1^{n-1}\right\|}{\|U_1^n\|}, \tag{5.3}$$

$$e_{U_2}^n = \frac{\left\|U_2^n - U_2^{n-1}\right\|}{\|U_2^n\|}. \tag{5.4}$$

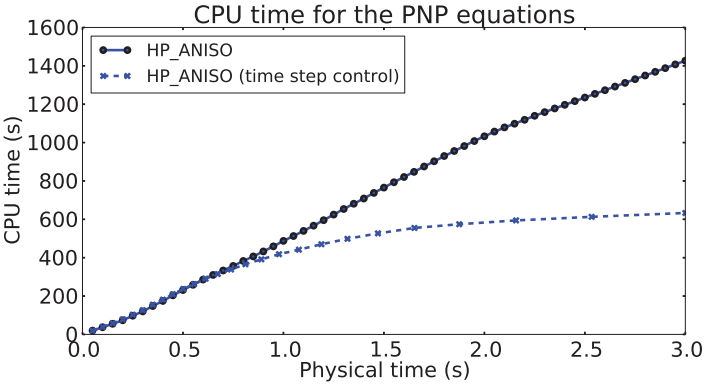

Figure 5.10: Cumulative CPU times as a function of physical time for HP_ANISO with and without time step adaptivity. The markers on the graphs indicate the time steps.

The relative changes to control the time step are calculated as follows:

$$e^n = \max\left\{e_c^n,\ e_\varphi^n,\ e_{U_1}^n,\ e_{U_2}^n\right\}. \tag{5.5}$$

If $e^n < \delta$ where $\delta > 0$ is a defined tolerance, then the time step for the next iteration is increased smoothly to

$$\delta\tau^{n+1} = \left(\frac{e^{n-1}}{e^n}\right)^{k_P} \left(\frac{\delta}{e^n}\right)^{k_I} \left[\frac{\left(e^{n-1}\right)^2}{e^n e^{n-2}}\right]^{k_D} \delta\tau^n, \tag{5.6}$$

where parameters are [82]:

$$k_p = 0.075, \quad k_I = 0.175, \quad k_D = 0.01. \tag{5.7}$$

The tolerance δ was set to $\delta = 0.25$ in the current optimization case. At this time, the implementation does not support adaptive time stepping if $e^n \geq \delta$. However, the implementation of advanced adaptive higher-order time-stepping methods is in progress. First, the optimization calculations were carried out only for the PNP system of equations, i.e. $e^n = \max\left\{e_c^n,\ e_\varphi^n\right\}$. The calculated e_c^n and e_φ^n are shown in Figure 5.8. The PNP problem size and computing time with and without time step control are shown in Figures 5.9 and 5.10. The CPU time was reduced more than two times when the time step control was employed.

Similarly, the problem size and CPU time with and without the time step control for PNP-Navier's equations (IPMC deformation calculation with $e^n = \max\left\{e_c^n,\ e_\varphi^n,\ e_{U_1}^n,\ e_{U_2}^n\right\}$ as defined in (5.5)) are shown in Figures 5.11

and 5.12 for 0.2 mm and 1.0 mm IPMCs. It can be seen that the computing time was reduced more than two times when the time step control was employed. At the same time, the problem size was not affected almost at all.

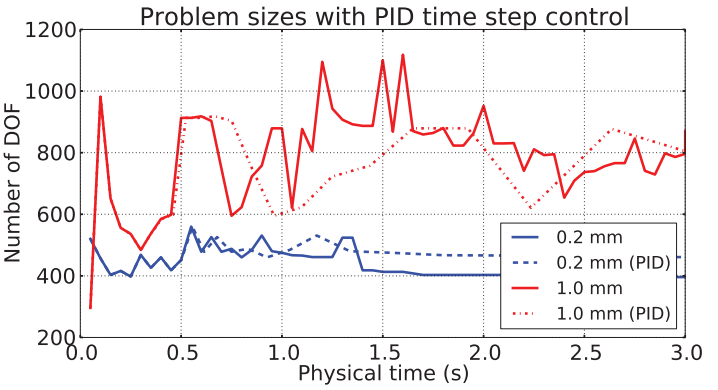

Figure 5.11: Problem sizes of 0.2 mm and 1.0 mm thick IPMCs with and without PID time step control.

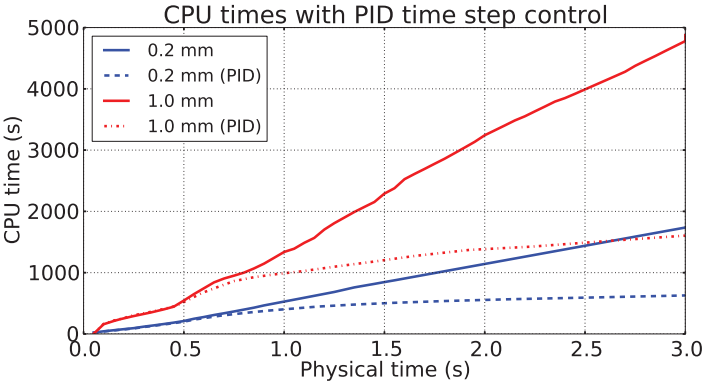

Figure 5.12: CPU times of 0.2 mm and 1.0 mm thick IPMCs with and without PID time step control.

5.3 Chapter conclusions

Due to *hp*-FEM automatic adaptivity, the PNP problem and more complex PNP-Navier's problem are well scalable for different geometry configurations. In the latter case, various IPMC thicknesses were modeled and

the problem size did not increase significantly with the change of thickness and aspect ratio of the calculation domain. However, the adaptivity can consume a lot of CPU time. It was shown that calculation times can be reduced more than twice by employing a simple PID controller based time step adaptivity.

CHAPTER 6

CONCLUSIONS

In this work the system of Poisson-Nernst-Planck (PNP) equations was solved using *hp*-finite element method with adaptive multi-mesh configuration. The weak form, residuals and the Jacobian matrix of the system were explicitly derived and implemented in Hermes *hp*-FEM time dependent adaptive solver. The solution for PNP problem with two field variables C and ϕ results in very different field gradients in the space and time. When using a conventional low order FEM, finding an optimal mesh for this type of problem such that both the error of the solution and problem size remain small throughout the time dependent solving process is difficult.

It was shown that using the time dependent adaptivity, multi-mesh configuration, and anisotropic *hp* refinements, the problem size remains very small throughout the solving process while maintaining a pre-set relative error of the solution. Namely, Hermes refinement mode HP_ANISO resulted in the smallest and fastest problem solution. Furthermore, using the multi-mesh configuration for the physical fields c and φ — scaled variables for C and ϕ, respectively — was justified. The adaptivity algorithm refined the meshes of φ and c and increased the polynomial degrees of the corresponding spaces differently. The mesh was significantly refined for c and also the maximum polynomial degree was varied in the range of $2 \dots 9$ whereas for φ, the maximum polynomial degree remained lower. So it is efficient to use multi-mesh in terms of the number of degrees of freedom.

Thereafter, IPMC electromechanical transduction was modeled by solving the system of PNP-Navier equations using the same method. The weak form, residuals and the Jacobian matrix of the system were again explicitly derived – so the result could be used with other finite element software

packages. Here, Hermes *hp*-FEM time dependent adaptive solver was again used. The solutions for the problem with four dimensionless field variables – cation concentration c, electric potential φ, x-directional displacement U_1, and y-directional displacement U_2 – result in very different field gradients in the space and time. It was shown that using the time dependent adaptivity, multi-mesh configuration, and anisotropic *hp*-refinements, the problem size remains very small throughout the solving process while maintaining a pre-set relative error of the solution. As in case of the PNP problem, Hermes refinement mode HP_ANISO resulted in the smallest and fastest problem solution. The meshes were significantly refined for c and φ and also the maximum polynomial degree was varied in the range of $2 \dots 8$ whereas for the displacement fields U_1 and U_2, the mesh variations were smaller; however, the polynomial degrees of the elements were increased where necessary.

Additionally, IPMC thicknesses were modeled and the problem size did not increase significantly with the change of thickness and aspect ratio of the calculation domain. However, the automatic adaptivity can consume a lot of CPU time. It was shown that calculation times can be reduced more than twice by employing a simple PID controller based time step adaptivity.

Conclusively, by using *hp*-FEM with adaptive multi-mesh configuration the problem size of the Nernst-Planck-Poisson equation system can be possibly reduced significantly while still maintaining prescribed precision of the solution. The same holds true for the more complicated problem: the Nernst-Planck-Poisson-Navier's system of equation for IPMC deformation. Based on those results, and this is yet to be demonstrated, that this is especially important when dealing with 3D problems in a large physical domain with non-uniform boundary conditions and different geometry configuration.

Bibliography

[1] K. J. Kim and M. Shahinpoor, "A novel method of manufacturing three-dimensional ionic polymer–metal composites (IPMCs) biomimetic sensors, actuators and artificial muscles," *Polymer*, vol. 43, no. 3, pp. 797 – 802, 2002.

[2] S. Nemat-Nasser and Y. Wu, "Comparative experimental study of ionic polymer–metal composites with different backbone ionomers and in various cation forms," *Journal of Applied Physics*, vol. 93, no. 9, pp. 5255–5267, 2003.

[3] S. Nemat-Nasser and S. Zamani, "Modeling of electrochemomechanical response of ionic polymer-metal composites with various solvents," *Journal of Applied Physics*, vol. 100, no. 6, p. 064310, 2006.

[4] D. J. Segalman, W. R. Witkowski, D. B. Adolf, and M. Shahinpoor, "Theory and application of electrically controlled polymeric gels," *Smart Materials and Structures*, vol. 1, no. 1, p. 95, 1992.

[5] M. Shahinpoor, "Conceptual design, kinematics and dynamics of swimming robotic structures using ionic polymeric gel muscles," *Smart Materials and Structures*, vol. 1, no. 1, p. 91, 1992.

[6] D. J. Segalman, W. R. Witkowski, R. R. Rao, D. B. Adolf, and M. Shahinpoor, "Finite element simulation of the 2D collapse of a polyelectrolyte gel disk," vol. 1916, pp. 14–21, SPIE, 1993.

[7] D. J. Segalman and W. R. Witkowski, "Two-dimensional finite element analysis of a polymer gel drug delivery system," *Materials Science and Engineering: C*, vol. 2, no. 4, pp. 243 – 249, 1995.

[8] M. Shahinpoor, "Electro-mechanics of bending of ionic polymeric gels as synthetic muscles for adaptive structures," in *Proceedings of the 1993 ASME Winter Annual Meeting*, vol. 35, p. 11, 1993.

[9] M. Shahinpoor, "Continuum electromechanics of ionic polymeric," *Smart Materials and Structures*, vol. 3, no. 3, p. 367, 1994.

[10] M. Shahinpoor, "Micro-electro-mechanics of ionic polymeric gels as electrically controllable artificial muscles," *Journal of Intelligent Material Systems and Structures*, vol. 6, no. 3, pp. 307–314, 1995.

[11] P. G. de Gennes, K. Okumura, M. Shahinpoor, and K. J. Kim, "Mechanoelectric effects in ionic gels," *EPL (Europhysics Letters)*, vol. 50, no. 4, p. 513, 2000.

[12] J. Y. Li and S. Nemat-Nasser, "Micromechanical analysis of ionic clustering in nafion perfluorinated membrane," *Mechanics of Materials*, vol. 32, no. 5, pp. 303 – 314, 2000.

[13] S. Nemat-Nasser, "Micromechanics of actuation of ionic polymer-metal composites," *Journal of Applied Physics*, vol. 92, no. 5, pp. 2899–2915, 2002.

[14] L. M. Weiland and D. J. Leo, "Electrostatic analysis of cluster response to electrical and mechanical loading in ionic polymers with cluster morphology," *Smart Materials and Structures*, vol. 13, no. 2, p. 323, 2004.

[15] Y. Bar-Cohen, *Electroactive polymer (EAP) actuators as artificial muscles: reality, potential, and challenges*. SPIE press, 2004.

[16] K. Mallavarapu and D. J. Leo, "Feedback control of the bending response of ionic polymer actuators," *Journal of Intelligent Material Systems and Structures*, vol. 12, no. 3, pp. 143–155, 2001.

[17] J. W. Paquette, K. J. Kim, and D. Kim, "Low temperature characteristics of ionic polymer–metal composite actuators," *Sensors and Actuators A: Physical*, vol. 118, no. 1, pp. 135 – 143, 2005.

[18] J. W. Paquette, K. J. Kim, D. Kim, and W. Yim, "The behavior of ionic polymer–metal composites in a multi-layer configuration," *Smart Materials and Structures*, vol. 14, no. 5, p. 881, 2005.

[19] D. Kim and K. J. Kim, "Experimental investigation on electrochemical properties of ionic polymer–metal composite," *Journal of Intelligent Material Systems and Structures*, vol. 17, no. 5, pp. 449–454, 2006.

[20] D. Kim, K. J. Kim, J. do Nam, and V. Palmre, "Electro-chemical operation of ionic polymer–metal composites," *Sensors and Actuators B: Chemical*, vol. 155, no. 1, pp. 106 – 113, 2011.

[21] M. Anton, M. Kruusmaa, A. Aabloo, and A. Punning, "Validating usability of ionomeric polymer-metal composite actuators for real world applications," in *Intelligent Robots and Systems, 2006 IEEE/RSJ International Conference on*, pp. 5441–5446, oct. 2006.

[22] M. Anton, A. Aabloo, A. Punning, and M. Kruusmaa, "A mechanical model of a non-uniform ionomeric polymer metal composite actuator," *Smart Materials and Structures*, vol. 17, no. 2, p. 025004, 2008.

[23] K. J. Kim, W. Yim, J. W. Paquette, and D. Kim, "Ionic polymer-metal composites for underwater operation," *Journal of Intelligent Material Systems and Structures*, vol. 18, no. 2, pp. 123–131, 2007.

[24] D. Dogruer, J. Lee, W. Yim, K. J. Kim, and D. Kim, "Fluid interaction of segmented ionic polymer–metal composites under water," *Smart Materials and Structures*, vol. 16, no. 2, p. S220, 2007.

[25] D. Kim and K. J. Kim, "Ionic polymer–metal composite actuators exhibiting self-oscillation," *Sensors and Actuators A: Physical*, vol. 137, no. 1, pp. 129–133, 2007.

[26] D. Kim and K. J. Kim, "A theoretical and experiment study for self-oscillatory ionic polymer–metal composite actuators," *Smart Materials and Structures*, vol. 16, no. 5, p. 1789, 2007.

[27] D. Kim, K. J. Kim, Y. Tak, D. Pugal, and I.-S. Park, "Self-oscillating electroactive polymer actuator," *Applied Physics Letters*, vol. 90, no. 18, pp. 184104 –184104–3, 2007.

[28] D. Pugal, H. Kasemagi, K. J. Kim, M. Kruusmaa, and A. Aabloo, "Finite element simulations of the bending of the IPMC sheet," in *Proceedings of SPIE* (Y. Bar-Cohen, ed.), vol. 6524, p. 65240B, 2007.

[29] D. Pugal, K. J. Kim, A. Punning, H. Kasemagi, M. Kruusmaa, and A. Aabloo, "A self-oscillating ionic polymer-metal composite bending actuator," *Journal of Applied Physics*, vol. 103, no. 8, p. 084908, 2008.

[30] R. Tiwari, K. J. Kim, and S. M. Kim, "Ionic polymer-metal composite as energy harvesters," *Smart Structures and Systems*, vol. 4, no. 5, pp. 549–563, 2008.

[31] J. Brufau-Penella, M. Puig-Vidal, P. Giannone, S. Graziani, and S. Strazzeri, "Characterization of the harvesting capabilities of an ionic polymer metal composite device," *Smart Materials and Structures*, vol. 17, no. 1, p. 015009, 2008.

[32] M. Shahinpoor and K. J. Kim, "Ionic polymer-metal composites: I. fundamentals," *Smart Materials and Structures*, vol. 10, no. 4, p. 819, 2001.

[33] J. Won, S. W. Choi, Y. S. Kang, H. Y. Ha, I.-H. Oh, H. S. Kim, K. T. Kim, and W. H. Jo, "Structural characterization and surface modification of sulfonated polystyrene–(ethylene–butylene)–styrene triblock proton exchange membranes," *Journal of Membrane Science*, vol. 214, no. 2, pp. 245 – 257, 2003.

[34] J.-H. Jeon, S.-P. Kang, S. Lee, and I.-K. Oh, "Novel biomimetic actuator based on speek and pvdf," *Sensors and Actuators B: Chemical*, vol. 143, no. 1, pp. 357 – 364, 2009.

[35] X.-L. Wang, I.-K. Oh, J. Lu, J. Ju, and S. Lee, "Biomimetic electro-active polymer based on sulfonated poly (styrene-b-ethylene-co-butylene-b-styrene)," *Materials Letters*, vol. 61, no. 29, pp. 5117 – 5120, 2007.

[36] X.-L. Wang, I.-K. Oh, and L. Xu, "Electro-active artificial muscle based on irradiation-crosslinked sulfonated poly(styrene-ran-ethylene)," *Sensors and Actuators B: Chemical*, vol. 145, no. 2, pp. 635 – 642, 2010.

[37] X.-L. Wang, I.-K. Oh, and T.-H. Cheng, "Electro-active polymer actuators employing sulfonated poly(styrene-ran-ethylene) as ionic membranes," *Polymer International*, vol. 59, no. 3, pp. 305–312, 2010.

[38] B. Akle, M. Bennett, D. Leo, K. Wiles, and J. McGrath, "Direct assembly process: a novel fabrication technique for large strain ionic polymer transducers," *Journal of Materials Science*, vol. 42, pp. 7031–7041, 2007.

[39] B. Akle, S. Nawshin, and D. Leo, "Reliability of high strain ionomeric polymer transducers fabricated using the direct assembly process," *Smart Materials and Structures*, vol. 16, no. 2, p. S256, 2007.

[40] T. Fukushima, K. Asaka, A. Kosaka, and T. Aida, "Fully plastic actuator through layer-by-layer casting with ionic-liquid-based bucky gel," *Angewandte Chemie International Edition*, vol. 44, no. 16, pp. 2410–2413, 2005.

[41] K. Mukai, K. Asaka, K. Kiyohara, T. Sugino, I. Takeuchi, T. Fukushima, and T. Aida, "High performance fully plastic actuator based on ionic-liquid-based bucky gel," *Electrochimica Acta*, vol. 53, no. 17, pp. 5555 – 5562, 2008.

[42] K. Mukai, K. Asaka, T. Sugino, K. Kiyohara, I. Takeuchi, N. Terasawa, D. N. Futaba, K. Hata, T. Fukushima, and T. Aida, "Highly conductive sheets from millimeter-long single-walled carbon nanotubes and ionic liquids: Application to fast-moving, low-voltage electromechanical actuators operable in air," *Advanced Materials*, vol. 21, no. 16, pp. 1582–1585, 2009.

[43] F. Pérez-Caballero, A.-L. Peikolainen, M. Uibu, R. Kuusik, O. Volobujeva, and M. Koel, "Preparation of carbon aerogels from 5-methylresorcinol–formaldehyde gels," *Microporous and Mesoporous Materials*, vol. 108, no. 1–3, pp. 230 – 236, 2008.

[44] V. Palmre, E. Lust, A. Janes, M. Koel, A.-L. Peikolainen, J. Torop, U. Johanson, and A. Aabloo, "Electroactive polymer actuators with carbon aerogel electrodes," *J. Mater. Chem.*, vol. 21, pp. 2577–2583, 2011.

[45] J. Torop, M. Arulepp, J. Leis, A. Punning, U. Johanson, V. Palmre, and A. Aabloo, "Nanoporous carbide-derived carbon material-based linear actuators," *Materials*, vol. 3, no. 1, pp. 9–25, 2009.

[46] V. Palmre, D. Brandell, U. Mäeorg, J. Torop, O. Volobujeva, A. Punning, U. Johanson, M. Kruusmaa, and A. Aabloo, "Nanoporous carbon-based electrodes for high strain ionomeric bending actuators," *Smart Materials and Structures*, vol. 18, no. 9, p. 095028, 2009.

[47] J. Torop, V. Palmre, M. Arulepp, T. Sugino, K. Asaka, and A. Aabloo, "Flexible supercapacitor-like actuator with carbide-derived carbon electrodes," *Carbon*, vol. 49, no. 9, pp. 3113 – 3119, 2011.

[48] J. Torop, T. Sugino, K. Asaka, A. Jänes, E. Lust, and A. Aabloo, "Nanoporous carbide-derived carbon based actuators modified with gold foil: Prospect for fast response and low voltage applications," *Sensors and Actuators B: Chemical*, vol. 161, no. 1, pp. 629 – 634, 2012.

[49] K. M. Newbury and D. J. Leo, "Linear electromechanical model of ionic polymer transducers -part i: Model development," *Journal of Intelligent Material Systems and Structures*, vol. 14, no. 6, pp. 333–342, 2003.

[50] C. Bonomo, L. Fortuna, P. Giannone, and S. Graziani, "A circuit to model the electrical behavior of an ionic polymer-metal composite,"

Circuits and Systems I: Regular Papers, IEEE Transactions on, vol. 53, no. 2, pp. 338 – 350, 2006.

[51] C. Bonomo, L. Fortuna, P. Giannone, S. Graziani, and S. Strazzeri, "A nonlinear model for ionic polymer metal composites as actuators," *Smart Materials and Structures*, vol. 16, no. 1, p. 1, 2007.

[52] R. Caponetto, G. Dongola, L. Fortuna, S. Graziani, and S. Strazzeri, "A fractional model for IPMC actuators," in *Instrumentation and Measurement Technology Conference Proceedings, 2008. IMTC 2008. IEEE*, pp. 2103 –2107, may 2008.

[53] P. Brunetto, L. Fortuna, S. Graziani, and S. Strazzeri, "A model of ionic polymer–metal composite actuators in underwater operations," *Smart Materials and Structures*, vol. 17, no. 2, p. 025029, 2008.

[54] A. J. McDaid, K. C. Aw, E. Haemmerle, and S. Q. Xie, "A conclusive scalable model for the complete actuation response for IPMC transducers," *Smart Materials and Structures*, vol. 19, no. 7, p. 075011, 2010.

[55] M. Kruusmaa, A. Hunt, A. Punning, M. Anton, and A. Aabloo, "A linked manipulator with ion-polymer metal composite (IPMC) joints for soft- and micromanipulation," in *Robotics and Automation, 2008. ICRA 2008. IEEE International Conference on*, pp. 3588 –3593, 2008.

[56] A. Punning, U. Johanson, M. Anton, M. Kruusmaa, and A. Aabloo, "A distributed model of IPMC," vol. 6927, p. 69270G, SPIE, 2008.

[57] A. Punning, U. Johanson, M. Anton, A. Aabloo, and M. Kruusmaa, "A distributed model of ionomeric polymer metal composite," *Journal of Intelligent Material Systems and Structures*, vol. 20, no. 14, pp. 1711–1724, 2009.

[58] P. J. C. Branco and J. A. Dente, "Derivation of a continuum model and its electric equivalent-circuit representation for ionic polymer–metal composite (IPMC) electromechanics," *Smart Materials and Structures*, vol. 15, no. 2, p. 378, 2006.

[59] G. Nishida, K. Takagi, B. Maschke, and T. Osada, "Multi-scale distributed parameter modeling of ionic polymer-metal composite soft actuator," *Control Engineering Practice*, vol. 19, no. 4, pp. 321 – 334, 2011.

[60] S. Nemat-Nasser and J. Y. Li, "Electromechanical response of ionic polymer-metal composites," *Journal of Applied Physics*, vol. 87, no. 7, pp. 3321–3331, 2000.

[61] K. Asaka and K. Oguro, "Bending of polyelectrolyte membrane platinum composites by electric stimuli: Part ii. response kinetics," *Journal of Electroanalytical Chemistry*, vol. 480, no. 1–2, pp. 186 – 198, 2000.

[62] M. Porfiri, "Charge dynamics in ionic polymer metal composites," *Journal of Applied Physics*, vol. 104, no. 10, p. 104915, 2008.

[63] Z. Chen and X. Tan, "A control-oriented and physics-based model for ionic polymer–metal composite actuators," *Mechatronics, IEEE/ASME Transactions on*, vol. 13, no. 5, pp. 519 –529, 2008.

[64] T. Wallmersperger, B. J. Akle, D. J. Leo, and B. Kröplin, "Electrochemical response in ionic polymer transducers: An experimental and theoretical study," *Composites Science and Technology*, vol. 68, no. 5, pp. 1173 – 1180, 2008.

[65] B. J. Akle, W. Habchi, T. Wallmersperger, E. J. Akle, and D. J. Leo, "High surface area electrodes in ionic polymer transducers: Numerical and experimental investigations of the electro-chemical behavior," *Journal of Applied Physics*, vol. 109, no. 7, p. 074509, 2011.

[66] J. Heinbockel, *Introduction to tensor calculus and continuum mechanics*. Trafford Publishing, 2001.

[67] D. Pugal, K. J. Kim, and A. Aabloo, "An explicit physics-based model of ionic polymer-metal composite actuators," *Journal of Applied Physics*, vol. 110, no. 8, p. 084904, 2011.

[68] D. Pugal, K. J. Kim, K. K. Leang, and V. Palmre, "Modeling and designing IPMCs for twisting motion: electromechanical and mechanoelectrical transduction," in *Proceedings of SPIE* (Y. Bar-Cohen and F. Carpi, eds.), vol. 7976, p. 79761S, 2011.

[69] D. Pugal, K. J. Kim, and A. Aabloo, "Modeling the transduction of IPMC in 3D configurations," in *Proceedings of SPIE*, vol. 7644, pp. 76441T–76441T–9, 2010.

[70] P. Solin, K. Segeth, and I. Dolezel, *Higher-Order Finite Element Methods*. Chapman & Hall / CRC Press, 2003.

[71] L. Dubcova, P. Solin, G. Hansen, and H. Park, "Comparison of multimesh *hp*-FEM to interpolation and projection methods for spatial coupling of thermal and neutron diffusion calculations," *Journal of Computational Physics*, vol. 230, no. 4, pp. 1182 – 1197, 2011.

[72] I. Babuška and M. Suri, "The p and h-p versions of the finite element method, basic principles and properties," *SIAM Review*, vol. 36, no. 4, pp. 578–632, 1994.

[73] G. E. Karniadakis and S. J. Sherwin, *Spectral/hp element methods for CFD*. Oxford University Press, 1999.

[74] L. Demkowicz, *Computing with hp-Adaptive Finite Elements: Volume 1 One and Two Dimensional Elliptic and Maxwell problems*. CRC Press, 2006.

[75] P. Solin, D. Andrs, J. Cerveny, and M. Simko, "Pde-independent adaptive *hp*-FEM based on hierarchic extension of finite element spaces," *Journal of computational and applied mathematics*, vol. 233, no. 12, pp. 3086–3094, 2010.

[76] P. Solin, J. Cerveny, L. Dubcova, and D. Andrs, "Monolithic discretization of linear thermoelasticity problems via adaptive multimesh *hp*-FEM," *Journal of Computational and Applied Mathematics*, vol. 234, no. 7, pp. 2350 – 2357, 2010.

[77] P. Solin, L. Dubcova, and J. Kruis, "Adaptive *hp*-FEM with dynamical meshes for transient heat and moisture transfer problems," *Journal of Computational and Applied Mathematics*, vol. 233, no. 12, pp. 3103 – 3112, 2010.

[78] L. Dubcova, P. Solin, J. Cerveny, and P. Kus, "Space and time adaptive two-mesh *hp*-finite element method for transient microwave heating problems," *Electromagnetics*, vol. 30, no. 1-2, pp. 23–40, 2010.

[79] M. Z. Bazant, K. Thornton, and A. Ajdari, "Diffuse-charge dynamics in electrochemical systems," *Phys. Rev. E*, vol. 70, no. 2, p. 021506, 2004.

[80] D. Pugal, A. Aabloo, and K. J. Kim, "Dynamic surface resistance model of IPMC," in *Proceedings of SPIE* (Z. Ounaies and J. Li, eds.), vol. 7289, p. 72891E, 2009.

[81] D. Pugal, P. Solin, K. J. Kim, and A. Aabloo, "Modeling ionic polymer-metal composites with space-time adaptive multimesh *hp*-FEM," *Communications in Computational Physics*, vol. 11, no. 1, pp. 249–270, 2012.

[82] A. M. P. Valli, G. F. Carey, and A. Coutinho, "Control strategies for timestep selection in simulation of coupled viscous flow and heat transfer," *Communications in Numerical Methods in Engineering*, vol. 18, no. 2, pp. 131–139, 2002.

ACKNOWLEDGMENTS

I would like to express my sincere gratitude to my advisors, Dr. Alvo Aabloo and Dr. Kwang Kim for their guidance and valuable advice. This dissertation would not have been possible without their support throughout the years I have been working on IPMC research. I'm also very grateful to Dr. Pavel Solin for introducing me the *hp*-FEM and his invaluable help and guidance in the research. I am very grateful for my opponents for taking their time and effort to read my work and provide interesting discussions. Also, I'd like to thank Dr. Kalev Tarkpea for getting me interested in joining the Physics Department of University of Tartu, to begin with. I would like to thank my former colleagues, in no particular order, Dr. Andres Punning, Dr. Maarja Kruusmaa, Dr. Viljar Palmre, Dr. Madis Listak, and Dr. Heiki Kasemägi, for collaboration throughout the years.

I acknowledge support from National Science Foundation grant #0713075, Office of Naval Research grant N00014091218, and Archimedes Foundation, Kristjan Jaak Scholarship programme.

My special thanks go to my dear wife Kersti and my parents for their continual support. I would also like to thank all my former colleagues at Cybernetica AS for their encouragement.

SUMMARY IN ESTONIAN

IPMC MATERJALI *hp*-FEM MUDEL

Ioonjuhtivaid polümeer-metall komposiitmaterjale (edaspidi lühendatud IPMC ehk *ionic polymer-metal composite*) on uuritud juba vähemalt kaks aastakümmet nende huvipakkuvate omaduste tõttu. Võimalikeks kasutusaladeks on vaiksed aktuaatorid või sensorid. IPMC eelised teiste elektroaktiivsete polümeeride ees on töötamine madalal pingel (1...5V), suur paindeulatus, ja toimimine veekeskkonnas. Kuigi põhiliselt on uuritud materjalide omadusi aktuaatoritena, on hiljuti materjalide sensoromadused rohkem tähelepanu saanud. Et materjali toimimisest aru saada ning seda kirjeldada erinevate rakenduste tarbeks, on vajalik füüsikal baseeruvat mudelit. Sellest lähtuvalt on välja töötatud Poisson-Nernst-Planck-Navier võrranditel baseeruva IPMC mudel. See baseerub füüsikalistel printsiipidest, ehk et saab kasutada võimalikult palju mõõdetavaid suurusi ääretingimustena (nagu materjali paindumine, rakendatud pinge jne). Lisaks on oluline, et meetod millel mudel baseerub, oleks efektiivne ning võimaldaks arvutusi väikese või vähemalt teadaoleva maksimaalse arvutusveaga. Käesoleva töö keskendub peamiselt just arvutusmeetodil ja annab ülevaate uudsest *hp*-FEM (*finite element method*) ehk *hp* lõplike elementide meetodist ja sellel baseeruvast IPMC mudelist. Kõigepealt on täielikult tuletatud võrrandid ja nende integraalne esitus Newtoni meetodi jaoks. Seejärel antakse lühike ülevaade *hp*-FEM meetodist adaptiivse väljapõhise võrguga ning kogu süsteemi Jakobiaani tuletus *hp*-FEM tarkvara Hermes jaoks. On näidatud kuidas automaatne adaptiivne *hp*-FEM võimaldab probleemi suuruse hoida väiksena (süsteemi vabadusastmeid ja kasutatud mälu silmas pidades). Kõige pealt on lahendatud Poisson-Nernst-Plancki võrrandisüsteem ja on käsitletud

erinevaid adaptiivusalgoritme. Üks huvitav tulemus on, et adaptiivsed algoritmid võimaldavad lahendada probleemi tingimustel, kus Debye pikkus jääb nanomeetri suurusjärku – seda süsteemis mille mõõtmed on millimeetri skaalas. Nendest tulemustest lähtuvalt esitatakse lahendus terve Poisson-Nernst-Planck-Navier võrrandite süsteemile IPMC paindumise arvutustes. Taaskord on lõplikud võrrandid koos tuletuskäiguga esitatud. Lisaks on analüüsitud suur hulk simulatsiooni tulemusi arvutusprobleemi suurust ja kulutatud arvutusaega silmas pidades ja sellest lähtuvalt leitud parim adaptiivuse algoritm seda liiki probleemide jaoks. On ka näidatud kuidas meetod võimaldab arvutusdomeeni geomeetriat arvesse võtta – domeeni pikkuse ja laiuse suhtest tulenevad ääreefektid on automaatselt arvutustes käsitletud. Kokkuvõtteks, käesolevas töös on detailselt kirjeldatud kuidas kasutades uudne *hp*-FEM meetod koos adaptiivsete algoritmide ja väljapõhise võrguga võimaldab Nernst-Planck-Poisson-Navier probleemi lahendada efektiivselt, samal ajal hoides lahenduse arvutusvea etteseatud piirides.

PUBLICATIONS

CURRICULUM VITAE

Personal data

Name	Deivid Pugal
Contact	david.pugal@gmail.com
More info	http://www.davidpugal.com

Education

2008–	University of Tartu, Ph.D. candidate in Physics
2008–2012	University of Nevada, Reno, Ph.D. in Mechanical Engineering
2005–2008	University of Tartu, MSc in Applied Physics
2002–2005	University of Tartu, BA in Applied Physics
1999–2002	CRJG, high school

Employment

2012–	OSIsoft LLC, software engineer
2005–2012	Cybernetica AS, software architect
2005–2008	Cybernetica AS, software developer
2004–2005	Heino Eller Music Shool, IT systems administrator

ELULOOKIRJELDUS

Isikuandmed

Nimi	Deivid Pugal
Kontaktandmed	david.pugal@gmail.com
Lisainfo	http://www.davidpugal.com

Haridustee

2008–	Tartu Ülikool, füüsika doktorant
2008–2012	Nevada Ülikool, Reno, doktor mehaanikas
2005–2008	Tartu Ülikool, magister rakendusfüüsikas
2002–2005	Tartu Ülikool, bakalaureus rakendusfüüsikas
1999–2002	CRJG, keskharidus

Teenistuskäik

2012–	OSIsoft, tarkvarainsener
2005–2012	Cybernetica AS, tarkvaraarhitekt
2005–2008	Cybernetica AS, tarkvaraarendaja
2004–2005	Heino Elleri nim. Muusikakool, IT süsteemide administraator

DISSERTATIONES PHYSICAE UNIVERSITATIS TARTUENSIS

1. **Andrus Ausmees.** XUV-induced electron emission and electron-phonon interaction in alkali halides. Tartu, 1991.
2. **Heiki Sõnajalg.** Shaping and recalling of light pulses by optical elements based on spectral hole burning. Tartu, 1991.
3. **Sergei Savihhin.** Ultrafast dynamics of F-centers and bound excitons from picosecond spectroscopy data. Tartu, 1991.
4. **Ergo Nõmmiste.** Leelishalogeniidide röntgenelektronemissioon kiiritamisel footonitega energiaga 70–140 eV. Tartu, 1991.
5. **Margus Rätsep.** Spectral gratings and their relaxation in some low-temperature impurity-doped glasses and chrystals. Tartu, 1991.
6. **Tõnu Pullerits.** Primary energy transfer in photosynthesis. Model calculations. Tartu, 1991.
7. **Olev Saks.** Attoampri diapasoonis voolude mõõtmise füüsikalised alused. Tartu, 1991.
8. **Andres Virro.** AlGaAsSb/GaSb heterostructure injection lasers. Tartu, 1991.
9. **Hans Korge.** Investigation of negative point discharge in pure nitrogen at atmospheric pressure. Tartu, 1992.
10. **Jüri Maksimov.** Nonlinear generation of laser VUV radiation for high-resolution spectroscopy. Tartu, 1992.
11. **Mark Aizengendler.** Photostimulated transformation of aggregate defects and spectral hole burning in a neutron-irradiated sapphire. Tartu, 1992.
12. **Hele Siimon.** Atomic layer molecular beam epitaxy of A^2B^6 compounds described on the basis of kinetic equations model. Tartu, 1992.
13. **Tõnu Reinot.** The kinetics of polariton luminescence, energy transfer and relaxation in anthracene. Tartu, 1992.
14. **Toomas Rõõm.** Paramagnetic H^{2-} and F^+ centers in CaO crystals: spectra, relaxation and recombination luminescence. Tallinn, 1993.
15. **Erko Jalviste.** Laser spectroscopy of some jet-cooled organic molecules. Tartu, 1993.
16. **Alvo Aabloo.** Studies of crystalline celluloses using potential energy calculations. Tartu, 1994.
17. **Peeter Paris.** Initiation of corona pulses. Tartu, 1994.
18. **Павел Рубин.** Локальные дефектные состояния в CuO_2 плоскостях высокотемпературных сверхпроводников. Тарту, 1994.
19. **Olavi Ollikainen.** Applications of persistent spectral hole burning in ultrafast optical neural networks, time-resolved spectroscopy and holographic interferometry. Tartu, 1996.
20. **Ülo Mets.** Methodological aspects of fluorescence correlation spectroscopy. Tartu, 1996.
21. **Mikhail Danilkin.** Interaction of intrinsic and impurity defects in CaS:Eu luminophors. Tartu, 1997.

22. **Ирина Кудрявцева.** Создание и стабилизация дефектов в кристаллах KBr, KCl, RbCl при облучении ВУФ-радиацией. Тарту, 1997.
23. **Andres Osvet.** Photochromic properties of radiation-induced defects in diamond. Tartu, 1998.
24. **Jüri Örd.** Classical and quantum aspects of geodesic multiplication. Tartu, 1998.
25. **Priit Sarv.** High resolution solid-state NMR studies of zeolites. Tartu, 1998.
26. **Сергей Долгов.** Электронные возбуждения и дефектообразование в некоторых оксидах металлов. Тарту, 1998.
27. **Kaupo Kukli.** Atomic layer deposition of artificially structured dielectric materials. Tartu, 1999.
28. **Ivo Heinmaa.** Nuclear resonance studies of local structure in $RBa_2Cu_3O_{6+x}$ compounds. Tartu, 1999.
29. **Aleksander Shelkan.** Hole states in CuO_2 planes of high temperature superconducting materials. Tartu, 1999.
30. **Dmitri Nevedrov.** Nonlinear effects in quantum lattices. Tartu, 1999.
31. **Rein Ruus.** Collapse of 3d (4f) orbitals in 2p (3d) excited configurations and its effect on the x-ray and electron spectra. Tartu, 1999.
32. **Valter Zazubovich.** Local relaxation in incommensurate and glassy solids studied by Spectral Hole Burning. Tartu, 1999.
33. **Indrek Reimand.** Picosecond dynamics of optical excitations in GaAs and other excitonic systems. Tartu, 2000.
34. **Vladimir Babin.** Spectroscopy of exciton states in some halide macro- and nanocrystals. Tartu, 2001.
35. **Toomas Plank.** Positive corona at combined DC and AC voltage. Tartu, 2001.
36. **Kristjan Leiger.** Pressure-induced effects in inhomogeneous spectra of doped solids. Tartu, 2002.
37. **Helle Kaasik.** Nonperturbative theory of multiphonon vibrational relaxation and nonradiative transitions. Tartu, 2002.
38. **Tõnu Laas.** Propagation of waves in curved spacetimes. Tartu, 2002.
39. **Rünno Lõhmus.** Application of novel hybrid methods in SPM studies of nanostructural materials. Tartu, 2002.
40. **Kaido Reivelt.** Optical implementation of propagation-invariant pulsed free-space wave fields. Tartu, 2003.
41. **Heiki Kasemägi.** The effect of nanoparticle additives on lithium-ion mobility in a polymer electrolyte. Tartu, 2003.
42. **Villu Repän.** Low current mode of negative corona. Tartu, 2004.
43. **Алексей Котлов.** Оксианионные диэлектрические кристаллы: зонная структура и электронные возбуждения. Tartu, 2004.
44. **Jaak Talts.** Continuous non-invasive blood pressure measurement: comparative and methodological studies of the differential servo-oscillometric method. Tartu, 2004.
45. **Margus Saal.** Studies of pre-big bang and braneworld cosmology. Tartu, 2004.

46. **Eduard Gerškevitš.** Dose to bone marrow and leukaemia risk in external beam radiotherapy of prostate cancer. Tartu, 2005.
47. **Sergey Shchemelyov.** Sum-frequency generation and multiphoton ionization in xenon under excitation by conical laser beams. Tartu, 2006.
48. **Valter Kiisk.** Optical investigation of metal-oxide thin films. Tartu, 2006.
49. **Jaan Aarik.** Atomic layer deposition of titanium, zirconium and hafnium dioxides: growth mechanisms and properties of thin films. Tartu, 2007.
50. **Astrid Rekker.** Colored-noise-controlled anomalous transport and phase transitions in complex systems. Tartu, 2007.
51. **Andres Punning.** Electromechanical characterization of ionic polymer-metal composite sensing actuators. Tartu, 2007.
52. **Indrek Jõgi.** Conduction mechanisms in thin atomic layer deposited films containing TiO_2. Tartu, 2007.
53. **Aleksei Krasnikov.** Luminescence and defects creation processes in lead tungstate crystals. Tartu, 2007.
54. **Küllike Rägo.** Superconducting properties of MgB_2 in a scenario with intra- and interband pairing channels. Tartu, 2008.
55. **Els Heinsalu.** Normal and anomalously slow diffusion under external fields. Tartu, 2008.
56. **Kuno Kooser.** Soft x-ray induced radiative and nonradiative core-hole decay processes in thin films and solids. Tartu, 2008.
57. **Vadim Boltrushko.** Theory of vibronic transitions with strong nonlinear vibronic interaction in solids. Tartu, 2008.
58. **Andi Hektor.** Neutrino Physics beyond the Standard Model. Tartu, 2008.
59. **Raavo Josepson.** Photoinduced field-assisted electron emission into gases. Tartu, 2008.
60. **Martti Pärs.** Study of spontaneous and photoinduced processes in molecular solids using high-resolution optical spectroscopy. Tartu, 2008.
61. **Kristjan Kannike.** Implications of neutrino masses. Tartu, 2008.
62. **Vigen Issahhanjan.** Hole and interstitial centres in radiation-resistant MgO single crystals. Tartu, 2008.
63. **Veera Krasnenko.** Computational modeling of fluorescent proteins. Tartu, 2008.
64. **Mait Müntel.** Detection of doubly charged higgs boson in the CMS detector. Tartu, 2008.
65. **Kalle Kepler.** Optimisation of patient doses and image quality in diagnostic radiology. Tartu, 2009.
66. **Jüri Raud.** Study of negative glow and positive column regions of capillary HF discharge. Tartu, 2009.
67. **Sven Lange.** Spectroscopic and phase-stabilisation properties of pure and rare-earth ions activated ZrO_2 and HfO_2. Tartu, 2010.
68. **Aarne Kasikov.** Optical characterization of inhomogeneous thin films. Tartu, 2010.

69. **Heli Valtna-Lukner.** Superluminally propagating localized optical pulses. Tartu, 2010.
70. **Artjom Vargunin.** Stochastic and deterministic features of ordering in the systems with a phase transition. Tartu, 2010.
71. **Hannes Liivat.** Probing new physics in e+e− annihilations into heavy particles via spin orientation effects. Tartu, 2010.
72. **Tanel Mullari.** On the second order relativistic deviation equation and its applications. Tartu, 2010.
73. **Aleksandr Lissovski.** Pulsed high-pressure discharge in argon: spectroscopic diagnostics, modeling and development. Tartu, 2010.
74. **Aile Tamm.** Atomic layer deposition of high-permittivity insulators from cyclopentadienyl-based precursors. Tartu, 2010.
75. **Janek Uin.** Electrical separation for generating standard aerosols in a wide particle size range. Tartu, 2011.
76. **Svetlana Ganina.** Hajusandmetega ülesanded kui üks võimalus füüsikaõppe efektiivsuse tõstmiseks. Tartu, 2011
77. **Joel Kuusk.** Measurement of top-of-canopy spectral reflectance of forests for developing vegetation radiative transfer models. Tartu, 2011.
78. **Raul Rammula**. Atomic layer deposition of HfO_2 – nucleation, growth and structure development of thin films. Tartu, 2011.
79. **Сергей Наконечный.** Исследование электронно-дырочных и интерстициал-вакансионных процессов в монокристаллах MgO и LiF методами термоактивационной спектроскопии. Тарту, 2011.
80. **Niina Voropajeva.** Elementary excitations near the boundary of a strongly correlated crystal. Tartu, 2011.
81. **Martin Timusk.** Development and characterization of hybrid electro-optical materials. Tartu, 2012, 106 p.
82. **Merle Lust.** Assessment of dose components to Estonian population. Tartu, 2012, 84 p.
83. **Karl Kruusamäe.** Deformation-dependent electrode impedance of ionic electromechanically active polymers. Tartu, 2012, 128 p.
84. **Liis Rebane.** Measurement of the $W \to \tau\nu$ cross section and a search for a doubly charged Higgs boson decaying to τ-leptons with the CMS detector. Tartu, 2012, 156 p.
85. **Jevgeni Šablonin.** Processes of structural defect creation in pure and doped MgO and NaCl single crystals under condition of low or super high density of electronic excitations. Tartu, 2013, 145 p.
86. **Riho Vendt**. Combined method for establishment and dissemination of the international temperature scale. Tartu, 2013, 108 p.
87. **Peeter Piksarv.** Spatiotemporal characterization of diffractive and non-diffractive light pulses. Tartu, 2013, 156 p.
88. **Anna Šugai.** Creation of structural defects under superhigh-dense irradiation of wide-gap metal oxides. Tartu, 2013, 108 p.

89. **Ivar Kuusik.** Soft X-ray spectroscopy of insulators. Tartu, 2013, 113 p.
90. **Viktor Vabson**. Measurement uncertainty in Estonian Standard Laboratory for Mass. Tartu, 2013, 134 p.
91. **Kaupo Voormansik.** X-band synthetic aperture radar applications for environmental monitoring. Tartu, 2014, 117 p.